Review Article

Andreas Braun*

Retrieval of digital elevation models from Sentinel-1 radar data – open applications, techniques, and limitations

https://doi.org/10.1515/geo-2020-0246
received December 16, 2020; accepted March 23, 2021

Abstract: With the launch of Sentinel-1 in 2014, a new era of openly accessible spaceborne radar imagery was begun, and its potential has been demonstrated throughout all fields of applications. However, while interferometric approaches to detect surface deformations are continuously being published, only a few studies address the derivation of digital elevation models (DEMs) from Sentinel-1 data. This is mainly because of the narrow orbital tube, which was primarily designed for subsidence measurements using differential interferometry. Nonetheless, the technical conditions are provided for successful applications involving DEM generation. These are outlined in the first part of this article with a focus on potential error sources and the impact of the most important constraints, namely, temporal and perpendicular baselines. The second part evaluates 21 studies on this topic, their aims, and how they dealt with error sources and the necessity of validation. These studies are then discussed based on the main challenges and potentials including how these can be tackled in the future to lay a solid foundation for scientific discourse.

Keywords: Sentinel-1, earth observation, remote sensing, digital elevation models, digital surface models, radar interferometry, InSAR, DEM generation, open source

1 Introduction

Among all data sources of geospatial information and analysis, digital elevation models (DEMs) hold a special role. They represent the continuous variations of the Earth's topography, primarily stored within cells of a regular raster grid, and are the main input for a large variety of applications, including geomorphologic mapping of landforms [1], numeric modeling of hydrologic runoff processes [2], viewshed and visibility computations [3], and many other forms of spatial analyses incorporating three or more dimensions [4,5].

Initially assessed through labor-intensive field surveys and analog photogrammetry [6], the term "digital terrain model" (DTM) was introduced by Miller and Laflamme in 1958 [7] to describe the topographic height of the Earth's surface. But with the development and utilization of airborne and satellite sensors, new methods for the consistent measurement of larger areas arose [8]. Digital photogrammetry makes use of images captured from multiple acquisition positions to exploit changes in the offset of object features for the derivation of elevation information [9,10]. As image features are recognized from image contrasts by mostly automatic matching techniques [11,12], this technique measures the height of the Earth's surface including potentially protruding objects, such as vegetation (e.g., forest canopies, crops) and artificial objects (e.g., urban areas and infrastructures). For such data, the term of digital surface models (DSMs) was created, which henceforth allowed the distinction between digitally derived ground and object heights. Two popular examples for globally computed DSMs, which were retrieved from photogrammetric processing, are the ASTER Global Digital Elevation Model (GDEM, processed from 1.2 million ASTER images acquired between 2001 and 2007 [13]) and the ALOS Global Digital Surface Model "ALOS World 3D 30m" (AW3D30, processed from around three million scenes of ALOS PRISM acquired between 2006 and 2011 [14]). Both are openly available at a spatial resolution of around 30 m [15,16]. With the invention of LiDAR and point-cloud processing techniques, both DTMs and DSMs can be derived from one data source alone since the beginning of the twenty-first century [17,18].

* **Corresponding author: Andreas Braun,** Department of Geosciences, Institute of Geography, University of Tübingen, 72070 Tübingen, Germany; Department of Geoinformatics –Z_GIS, University of Salzburg, 5020 Salzburg, Austria,
e-mail: an.braun@uni-tuebingen.de

As an alternative to airborne measurements and optical imagery, spaceborne synthetic aperture radar (SAR) sensors are employed to measure the Earth's elevation. The use of this side-looking system for the retrieval of height information has already been acknowledged since the 1970s [19]; however, its capabilities for topographic mapping based on stereoscopic methods applied to the amplitude, also called radargrammetry, yield images that are reportedly limited [20–22]. Moreover, its full potential lies in the exploitation of the phase information, which allows the measuring of topographic variation using radar interferometry (InSAR, [23–27]). The most prominent example is the Shuttle Radar Topography Mission (SRTM) conducted within 11 days in 2000 to produce a nearly global DEM at the spatial resolution of 30 m [28]. It is freely available [29] and has been used in countless studies throughout a wide range of disciplines [30,31]. In 2016, a DEM of global coverage with a spatial resolution of 12.5 m based on products acquired by the two radar satellites TerraSAR-X and TanDEM-X between 2011 and 2015 was released by the German Aerospace Center (DLR, [32,33]). As of now, it is the most up to date, detailed, and globally available DEM. It has been opened for free scientific use at a reduced spatial resolution of 90 m since 2019 [34]. One reason for the high vertical accuracies of both datasets (root-mean-square error (RMSE): SRTM <8 m [35] and TanDEM-X <1.4 m [36]) lies in the multitude of input acquisitions, which allowed the coverage of each part of the Earth several times and under different acquisition geometries and flight directions [37], and in case of TanDEM-X, data were captured at different parts of the season [32] to minimize errors resulting from seasonality and geometric distortions.

With the launch of Sentinel-1 by the European Space Agency (ESA) in 2014, a new and unprecedented period of openly available radar data were initiated within the Copernicus Programme, delivering an amount exceeding 12 TB of data per day [38]. This C-band radar mission, currently consisting of Sentinel-1A (S1A) and Sentinel-1B (S1B), acquires products in intervals of up to 6 days at a spatial resolution of 5×20 m (single look complex (SLC)), which can be used for interferometric analyses. However, the entire mission was primarily designed for differential radar interferometry (DInSAR; Figure 1c) to measure surface deformations between two or more acquisitions, which imposes limits upon its capabilities to derive DEMs [39,40]. Accordingly, studies on the derivation of absolute elevations or object heights are rare and often characterized by exaggerated expectations. Based on their expected life time of up to 10 years, and the already ongoing development of their successors, Sentinel-1C and Sentinel-1D, we currently anticipate many more years of continued acquisitions, thus justifying the evaluation of the present situation and the discussion of upcoming research needs and goals.

Therefore, the aim of this study is to provide an overview of the generation of DEMs with openly available Sentinel-1 data. Basic theories and concepts are outlined in Section 2.1, accompanied by a showcase example to underline the impact of different parameters on the quality of the derived DEM, followed by a presentation of open software packages and training resources (Section 2.2). Based on this background, a systematic literature

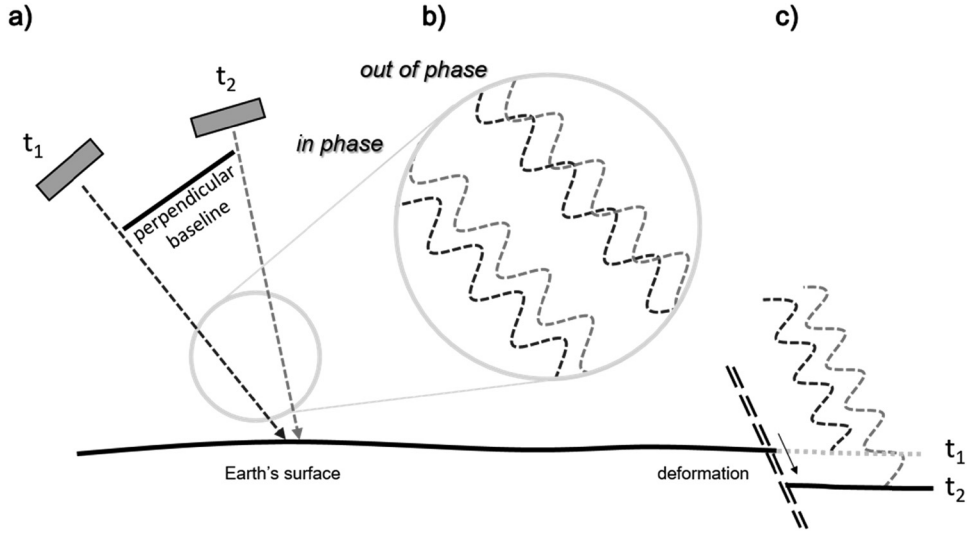

Figure 1: InSAR principles (adapted from Reference [197]). (a) InSAR geometry; (b) waves in detail; (c) DInSAR principle.

review is conducted to summarize existing studies, their aims, technical approaches, and the reported problems and limitations with respect to the retrieval of accurate surface heights. The article ends with a discussion of the gathered findings and identified research gaps, and an outlook on future challenges to shape the future development of techniques and applications based on the Sentinel-1 data.

2 Sentinel-1 interferometry

2.1 InSAR principles and parameters

2.1.1 Theoretic framework

The basic idea behind synthetic aperture radar interferometry (InSAR) is the combination of information provided by two different radar images, which have a known distance, the perpendicular baseline (Figure 1a). Based on the positions of both satellites and their perpendicular baseline, three-dimensional information of the Earth's surface can be retrieved by the different path lengths of the radar echo signals from a surface as received by both antennas [41,42]. In the case of SRTM, these images were acquired at the same time ($t_1 = t_2$) by two antennas, which were separated by a mast of 60 m length; this is also referred to as bistatic or single-pass interferometry. As the scattering mechanisms of the Earth's surface rarely do change within the time of data acquisition and the perpendicular baseline is constant, the retrieved signals are largely coherent (in-phase, Figure 1b), and the acquisition geometry can be precisely resolved for the topographic variations in the observed area [41]. The same bistatic principle is applied in the TanDEM-X mission, which consists of a constellation of two similar but independent satellites, which simultaneously acquire images within a helix-shaped orbit [32]. During its operation, their distance was changed in various phases to systematically analyze the impact of the perpendicular baseline on the retrieved information [43].

However, most radar satellites operate in a monostatic mode, which means that they do not have a tandem configuration, but utilize images acquired by the same antenna, but at two different times ($t_1 < t_2$). This approach is known as repeat-pass interferometry and is limited by the revisit rate of a satellite, which is defined at the interval at which the sensor recurs to the same position after orbiting the Earth [24]. For the Sentinel-1 satellite mission, this period is 12 days for each of the two satellites, but as they have the same configuration and a systematic offset, the revisit time can be reduced to 6 days when the images of S1A and S1B are combined. Repeat-pass interferometry enables the measuring of elevations based on the same principles as single-pass InSAR but is unavoidably susceptible to a number of error sources originating from potentially different conditions at the time of the acquisitions. These include receiver phase instabilities, incorrect estimates of the perpendicular baseline, atmospheric differences, as well as changes in altitude or land cover between the first and the second image [44]. While atmospheric and sensor-specific factors introduce patterns that can be easily misinterpreted as topographic variation [45], the problem of phase decorrelation leads to bad interferometric data quality in general, mostly over vegetated areas, which cannot be restored [24,46]. Short wavelengths are particularly prone to temporal decorrelation, such as those transmitted and received by the C-band of Sentinel-1 (5.405 GHz, corresponds to around 5.5 cm). This will be exemplified in the following sections.

2.1.2 Main processing steps

In the following, the derivation of DEMs from InSAR is briefly explained. However, as the well-established development of approaches for topographic mapping dates back into the 1980s, only the most important processing steps are explained, and the reader is advised to consult the given references for more detailed descriptions and mathematical elaborations. In turn, the presented methods and their parameters are calculated based on the data listed in Table 1 and illustrated by the maps shown in Figure 4.

In accord with the slant-looking geometry of every SAR measurement, signals transmitted by the antenna return to the sensor at different temporal delays, based on the distance R of the objects on the Earth's surface to the satellite [44]. As this signal propagates in a sinusoidal nature (Figure 2), the measured delay τ is equivalent to a phase change φ between the transmitted and the received signal [47]. As indicated in equation 1, φ is proportional to the two-way travel distance $2R$ divided by the transmitted wavelength λ.

$$\varphi = \frac{2\pi}{\lambda} \cdot 2R = \frac{\pi}{\lambda} \cdot R. \quad (1)$$

Due to differences regarding the spatial resolution of Sentinel-1 SLC products (5 × 20 m) and the scale of the wavelength (5.55 cm), the phase change between

Table 1: Datasets used in this study to illustrate the effect of different parameters

Type	Date	b_temp	b_perp	ID
Reference (dsc)	02.07.2019	—	—	S1B_IW_SLC__1SDV_20190702T032447_20190702T032514_016949_01FE47_69C5
Secondary A1	26.06.2019	6	146	S1A_IW_SLC__1SDV_20190626T032532_20190626T032559_027845_0324BF_8232
Secondary A2	14.06.2019	18	149	S1A_IW_SLC__1SDV_20190614T032531_20190614T032558_027670_031F87_5878
Secondary A3	08.06.2019	24	151	S1B_IW_SLC__1SDV_20190608T032445_20190608T032512_016599_01F3E2_AB78
Secondary A4	09.05.2019	54	168	S1A_IW_SLC__1SDV_20190509T032529_20190509T032556_027145_030F54_2BEA
Secondary A5	28.03.2019	96	144	S1B_IW_SLC__1SDV_20190328T032442_20190328T032517_015549_01D251_6DB4
Secondary B1	20.06.2019	12	67	S1B_IW_SLC__1SDV_20190620T032446_20190620T032513_016774_01F91A_EEA8
Secondary B2	02.06.2019	30	27	S1A_IW_SLC__1SDV_20190602T032530_20190602T032557_027495_031A40_BDE2
Reference (asc)	02.07.2019	—	—	S1A_IW_SLC__1SDV_20190702T151801_20190702T151829_027940_032792_1314
Secondary C1	26.06.2019	6	52	S1B_IW_SLC__1SDV_20190626T151735_20190626T151802_016869_01FBDB_E7BA

b_temp = temporal baseline; b_perp = perpendicular baseline.

neighboring pixels, representing only the last fraction of $2R$, looks random at first (Figure 3, left). However, when cross-multiplying the phase of the first image with the complex conjugate of the second image in a pixel-by-pixel manner, an interferogram is retrieved, which consists of phase variations φ as a result of topography φ_{topo}, the Earth's curvature φ_{flat}, surface deformation between both acquisitions φ_{disp}, atmospheric contributions φ_{atm}, and system-induced noise φ_{noise} (equation 2) [48] under the given acquisition geometry (Figure 3, right; Figure 4c) [25].

$$\varphi = \varphi_{\text{topo}} + \varphi_{\text{flat}} + \varphi_{\text{disp}} + \varphi_{\text{atm}} + \varphi_{\text{noise}}. \quad (2)$$

A mathematical description of this process, including the subtraction of the flat-earth phase φ_{flat} component (interferogram flattening), is given in previous studies [22,44,47]. However, the formation of an interferogram relies on the accurate stacking of the first (reference) and the second (secondary) images, so that the phase difference is calculated for the correct pixel pairs. This can be achieved at sub-pixel accuracy by methods of coregistration, which are based on cross-correlation and spectral diversity approaches [49–51]. This grants that the information of both images refers to the same object at the ground and that no errors are introduced at an early stage.

As presented by Hanssen [24], the main reasons for noise induced in interferograms are as follows:

- Changes of scattering mechanisms between both images (temporal decorrelation).
- Changes in the incidence angle between both acquisitions (baseline decorrelation).
- Penetration of the radar wave into mediums (volume decorrelation).
- Thermal noise and other antenna-related sources of bias.
- Additional processing-induced errors, such as low coregistration quality.

To estimate the quality of the interferogram throughout the image, the local coherence γ is calculated between the reference and the secondary image. It is a cross-correlation measure based on a defined window size as demonstrated in equation 3 and serves as a spatial indicator of the reliability and robustness of the later products derived from the interferogram [42,52]. In this equation, the amplitude of each pixel of the interferogram $|v|$ is proportional to the product of the amplitudes of the reference $|u_1|$ and the secondary image $|u_2|$, and E is the expected value of the random variable x [47,53].

$$\gamma = \frac{E[u_1 u_2^*]}{\sqrt{E[|u_1|^2]}\sqrt{E[|u_2|^2]}} = \frac{E[v]}{I}; \quad |\gamma| < 1. \quad (3)$$

The coherence ranges between 0 and 1, where large values indicate a high correlation between the reference and the secondary image, which is the case over urban areas and bare soils, while low values occur in areas of vegetation and other rapidly changing surfaces (Figure 4d). It helps to decide whether an area produces coherent (in-phase, Figure 1b) scattering. Although there is no universal threshold above which the phase information is considered usable, values between 0.1 and 0.4 are often used as a pragmatic solution to mask out noisy parts from the interferogram and to avoid errors becoming introduced during later steps [54,55]. However, it is important for the subsequent unwrapping of the interferogram that the remaining parts are still connected.

Although isolated patches of high coherence can be technically unwrapped correctly, the result for the full scene fails if they are not sufficiently connected over the entire image [24]. This is especially valid for the

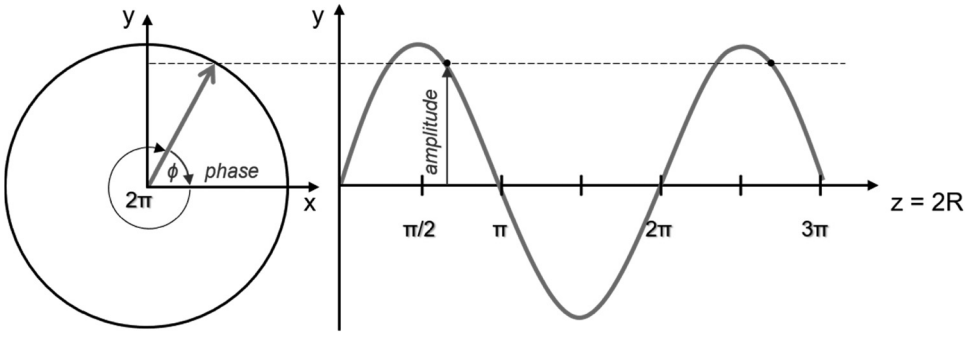

Figure 2: Amplitude and phase of a radar wave (adapted from Reference [197]).

derivation of digital surfaces, which form a continuum within the scene [56,57].

As shown in Figure 4c, each color cycle in the interferogram represents one phase difference between the reference and the secondary image. These patterns are also called fringes, where each fringe has a distance of 2π radians with respect to the employed wavelength of the system. With respect to equation 2 and the examples presented in Table 1 (A1), the amount of topographic height variations φ_{topo} represented by this 2π cycle is dependent on the wavelength λ (5.55 cm), the perpendicular baseline b_{perp} (−153 m), the range distance between the sensor and the Earth R (845 km), and the incidence angle θ (39°) as demonstrated in equation 4a [24,27]. If this equation is solved for the given example, one fringe cycle $H_{2\pi}$ represents 147.7 m of topographic difference (equation 4b), which is also known as the height ambiguity [48]. For the mapping of topography, smaller height ambiguities allow a more precise description of terrain features.

$$\varphi_{\text{topo}} = -\frac{4\pi}{\lambda} \cdot \frac{b_{\text{perp}}}{R \cdot \sin\theta} \cdot H. \tag{4a}$$

$$H_{2\pi} = -\frac{\lambda \cdot R \sin\theta}{2 \cdot b_{\text{perp}}} = -\frac{0.055 \cdot 8.45E5 \cdot \sin(39)}{2 \cdot -153} \tag{4b}$$

$$= 147.7 \text{ m}.$$

To convert this cyclic measure (also called the principal or wrapped phase) into a continuous measure, a wide range of phase unwrapping approaches have been proposed [58,59], and these integrate the phase at a pixel-by-pixel level over the entire image along closed paths, considering that phase differences greater than the principal interval of π cannot occur [47,60]. The result is a full phase representation of topographic variations as shown in Figure 4e. However, as mentioned earlier, this process is prone to errors induced by complex

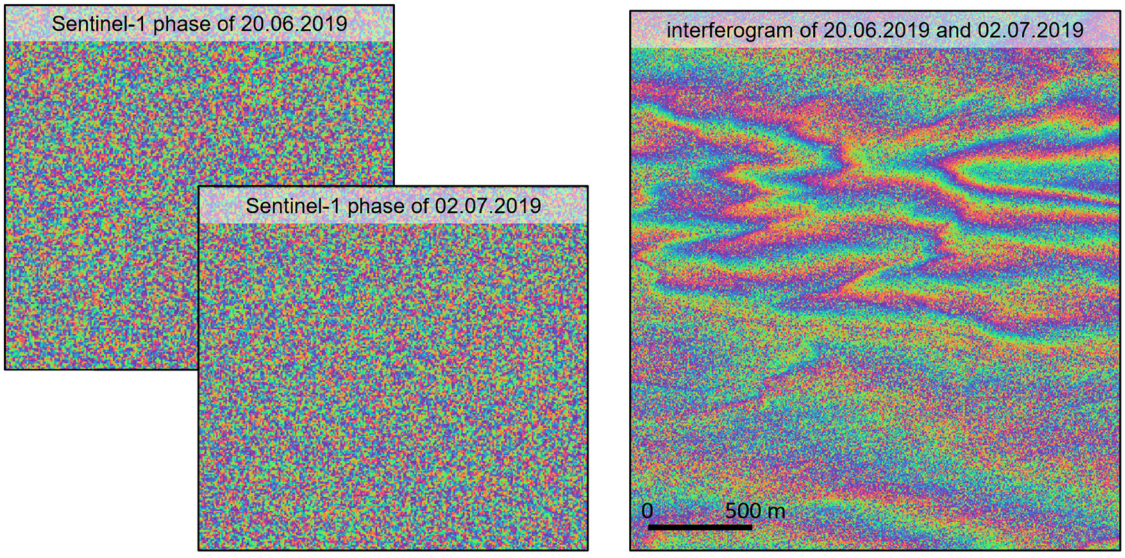

Figure 3: Combination of two complex phase products to an interferogram.

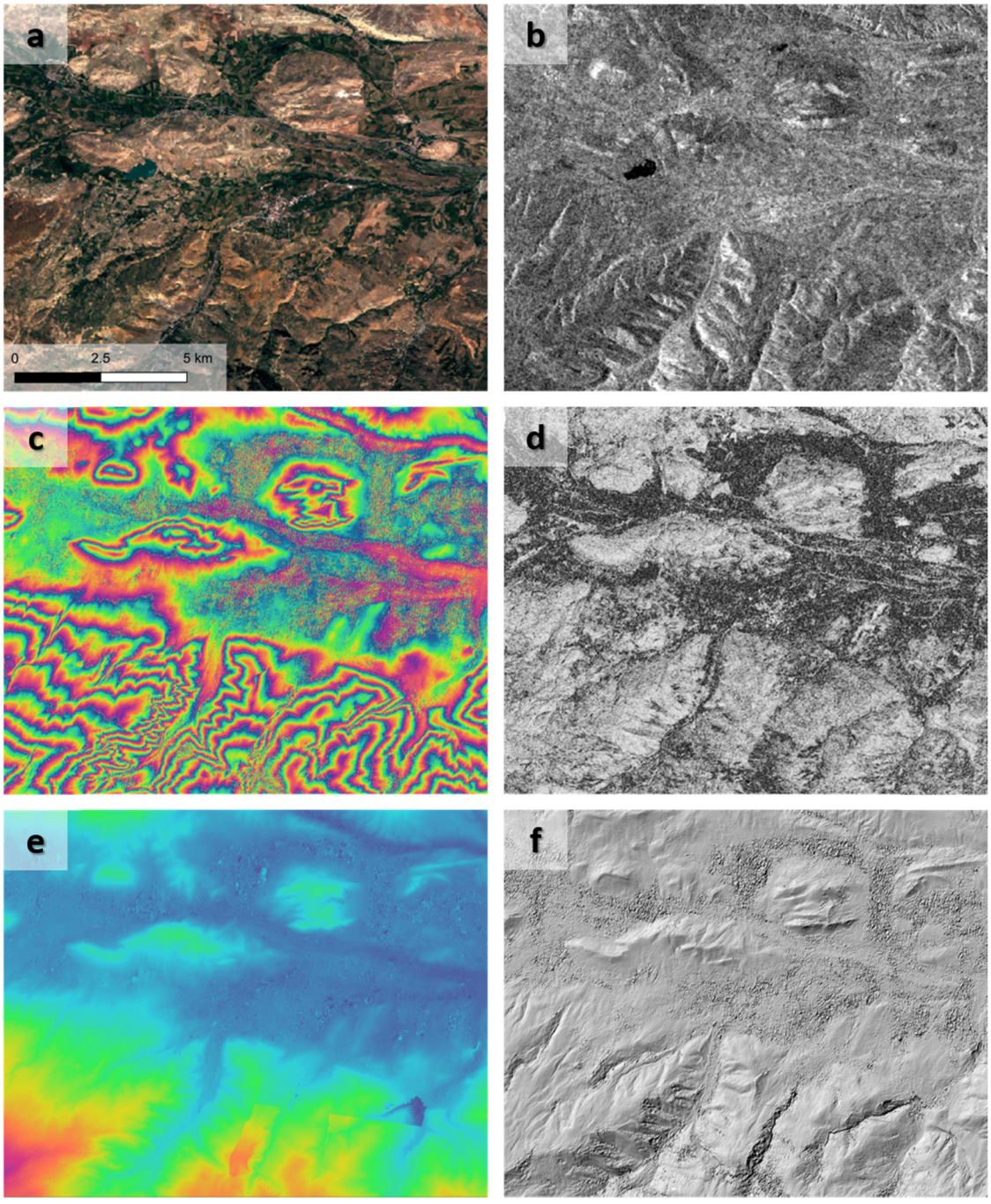

Figure 4: Steps of DEM generation with Sentinel-1: (a) Sentinel-2 image from 02.07.2019 (for visual reference), (b) Sentinel-1 image from 02.07.2019, (c) interferogram from 26.06.19 and 02.07.2019, (d) coherence image, (e) unwrapped interferogram, and (f) hillshade of the derived DEM. The extent is shown in Figure A1. This figure shows the modified Copernicus data.

topographies, phase noise in areas of low coherence, as well as by atmospheric artifacts [24,48,56]. Smaller amounts of noise can be tackled by specialized phase filters [61–65], but especially in interferograms with larger patches of low coherence, errors can be introduced in the form of phase jumps or entire trends superimposing the actual topographically induced phase variation [22]. Furthermore, based on the relative nature of InSAR measurements and the unavailability of *a priori* information about the terrain, it is worth mentioning that no ultimate solution to phase unwrapping exists, and it is always an approximation [44,60].

In a final step, the unwrapped phase is geocoded and translated into a geophysical unit, which represents the

height of the calculated surface over the spherical Earth [24]. This can be done by integrating the height of either surveyed reference points or extracted from an external DEM [66], but across-track approaches also exist, which are independent of a reference [67]. Finally, the retrieved heights are referenced to an ellipsoid (e.g., WGS84), projected into a coordinate reference system based on either geographical or UTM coordinates, and resampled to a uniform pixel spacing [22,66,68]. A potential result is shown as a hillshade representation in Figure 4f.

2.1.3 Impact of temporal baseline

As described in the previous sections, one major reason for phase decorrelation is the change of scattering mechanisms between the acquisition of the reference and the secondary image. Currently, Sentinel-1 is a mission employing two satellites, which allow the generation of repeat-pass interferograms with a temporal baseline of 6 days under best conditions. However, as land surfaces can rapidly change, this period is not ideal compared to the bistatic missions of SRTM and TanDEM-X. Given that the wavelength of Sentinel-1 is comparably short, vegetation areas are especially likely to lose their coherent scattering properties within a couple of seconds [54,69]. Therefore, it is impossible to retrieve reliable phase information on the height of forest stands or agricultural fields based on a single Sentinel-1 image pair [70]. These shortcomings were addressed in previous times when the temporal baseline between acquisitions of ERS-1 and ERS-2 was systematically reduced to 1 day [71] or images of ERS and ENVISAT of the same day were combined for DEM generation [72–74]. Yet, the limitations of volume decorrelation and increased sensitivity to tropospheric disturbance and water vapor persist for C-band systems [75,76].

To illustrate the impact of the temporal baseline on the quality of interferometric analyses, five interferograms were computed for one reference image (July 2, 2019) and secondary images acquired with a separation of 6 days (A1), 18 days (A2), 24 days (A3), 54 days (A4), and 96 days (A5) (Table 1). For reasons of consistency, all image pairs have a similar perpendicular baseline (discussed in Section 2.1.4).

As shown in Figure 5, a loss of coherence is observed with growing temporal baseline. On average, an extension of the temporal baseline from 6 to 18 days leads to a decrease of coherence of –19.2%. To put this observation into an environmental perspective, coherence was analyzed with respect to the main land cover classes in the area as retrieved from the Corine Land Cover 2018 dataset [77]. The largest relative decrease is observed for the nonforest vegetation areas (–30.6% from 6 to 18 days and –56.1 from 6 to 96 days), while urban areas are comparably robust at a high level (above 0.5). In turn, agricultural areas and water bodies already have low coherence values for very short temporal baselines and show a smaller relative decrease of only –20% over the entire period. The figure underlines that InSAR quality is highly sensitive to temporal decorrelation over natural surfaces, especially over areas of vegetation and water areas. While this relationship can be effectively exploited for multitemporal land cover mapping [78,79], the capabilities of Sentinel-1 for topographic mapping are severely limited in densely vegetated areas.

To visually underline the findings of Figure 5, the coherence products of different baselines, as well as the interferograms resulting from these combinations, are compared in Figure 6. It shows the city of Erzincan, Turkey, which is surrounded by agricultural and natural plains and framed by the *Esence* Mountains in the north and the *Mercan* Mountains in the south. Height differences between the city and the ridges in the selected extent are up to 1,000 m. The figure illustrates that the fringes are well aligned with the topographic conditions of the mountains and that the interferogram forms a consistent pattern in the plains. However, with increasing temporal baseline, these patterns suffer from decorrelation, caused by phenological changes due to the crop growth in the agricultural areas and seasonal changes over natural vegetation. This decorrelation strongly affects the interferogram quality, indicated by a higher amount of phase noise and less pronounced fringes. Most importantly, the different parts of the interferogram are no longer connected, which will lead to severe errors in the subsequent unwrapping, which relies on the steady integration of the continuous phase signal [60]. The results of the 6-day baseline image pair are presented in Section 2.1.4.

2.1.4 Impact of perpendicular baseline

From the perspective of the acquisition geometry, two points are crucial for the reliable retrieval of topographic information. First, the position of the satellites during the time of image acquisition must be known precisely. For Sentinel-1, this is granted by the provision of precise (or restituted) orbit information by the Copernicus Precise Orbit Determination (POD) Service [80]. These have an accuracy of 10 cm and are provided within a couple of days after image acquisition for non-time

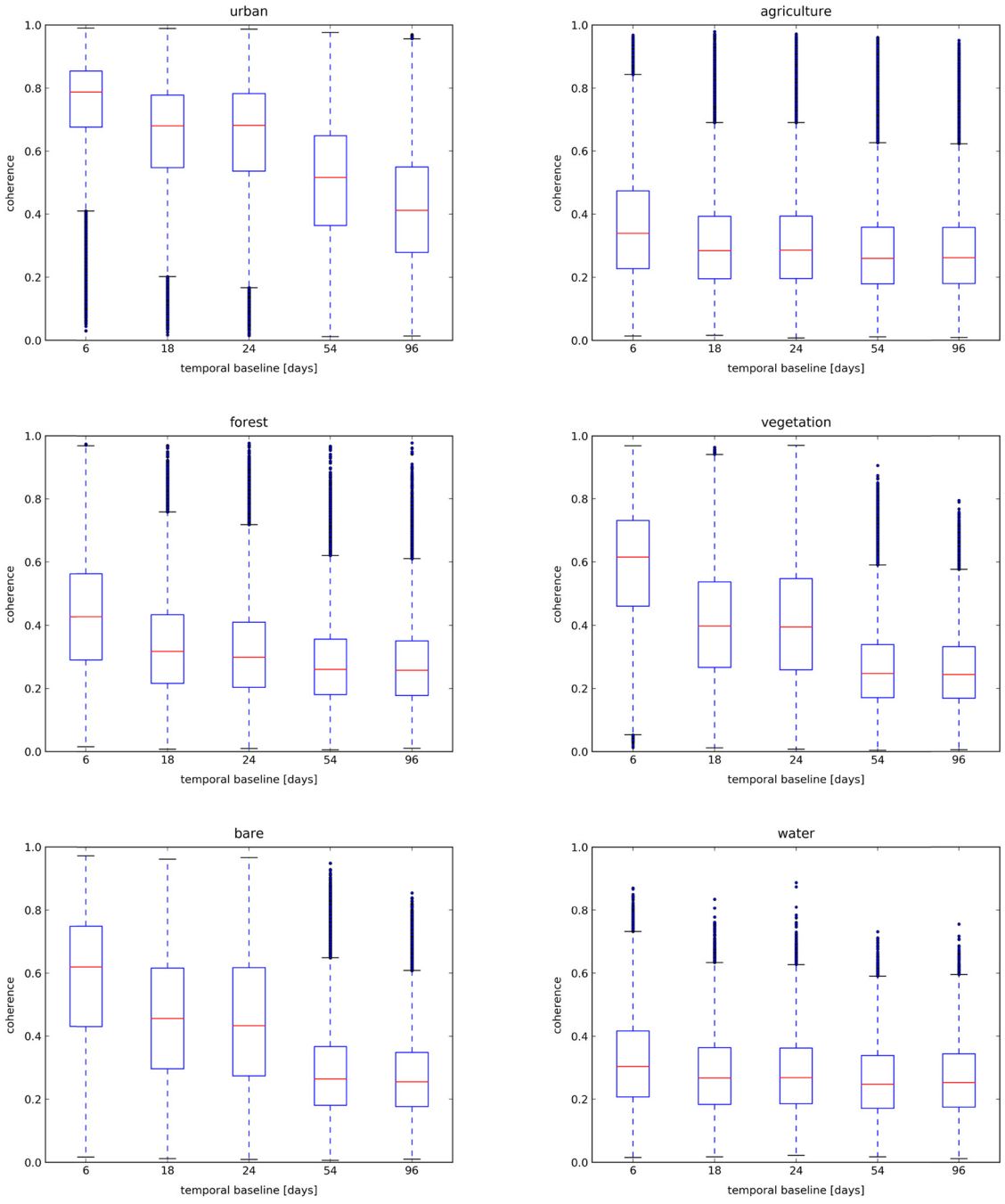

Figure 5: Loss of coherence of selected land cover classes for the investigated temporal baselines (shown Table 1).

critical products [81]. Their high accuracy was also reported for combinations of S1A and S1B to facilitate the use of 6-day temporal baseline pairs [82]. Second, the perpendicular baseline (Figure 1a) of the repeat-pass acquisition should be between 150 and 400 m to allow a precise description of topographic variations by the observed fringes [59]. However, as reported in Section 1, the orbital tube of Sentinel-1 was designed for differential interferometry, which requires small perpendicular baselines [83]. For the majority of image pairs within intervals of 6 or 12 days, perpendicular baselines are below 150 m and even smaller than 25 m in most of all cases [84]. A detailed evaluation of perpendicular baseline lengths with respect to the different orbits of S1A and S1B is given in the Sentinel-1 performance report of 2019 [85]. Referring to equation 4, perpendicular baselines between 25 and 50 m generate fringes with height ambiguities of 500 and 1,000 m of altitude. Interferograms of

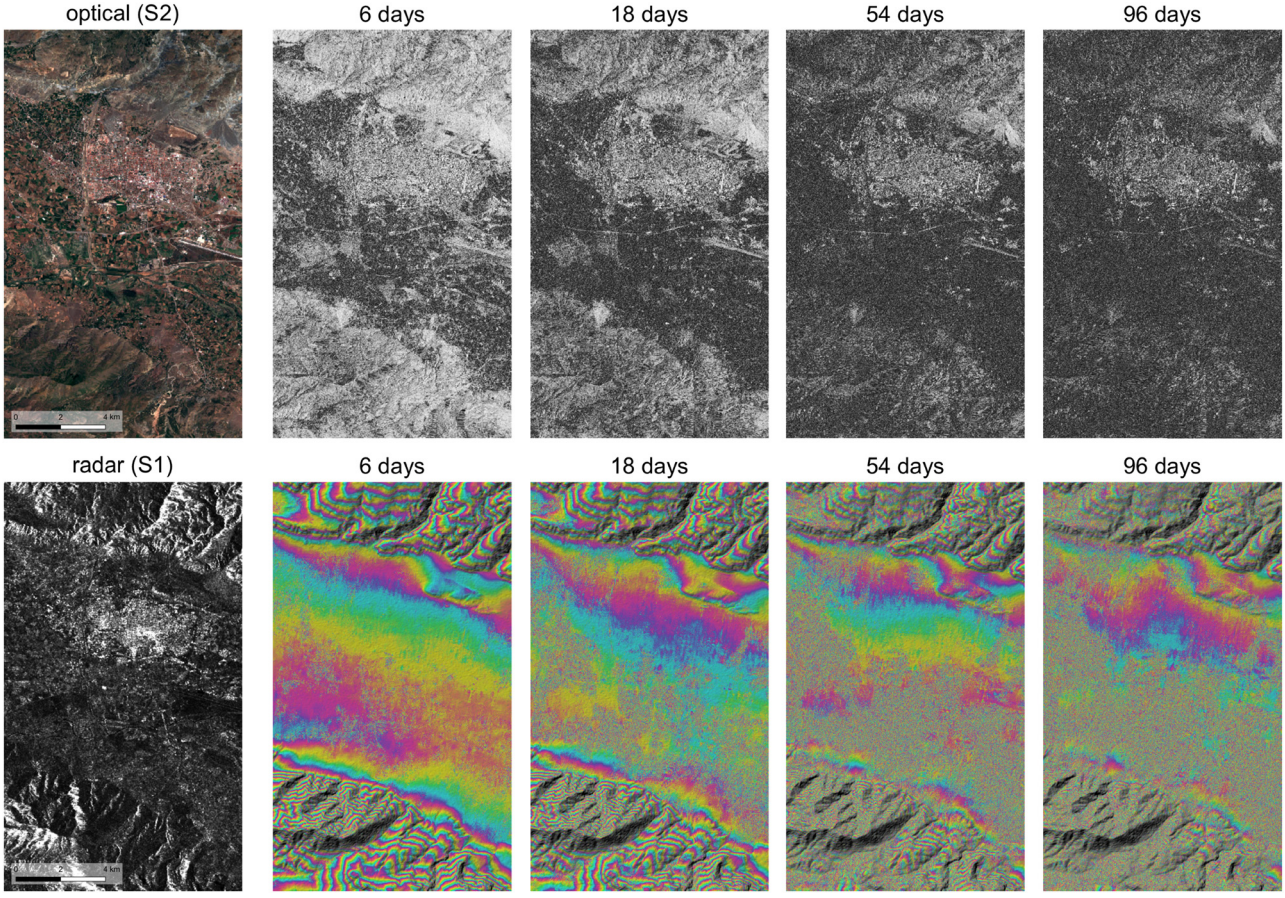

Figure 6: Coherence (top) and interferograms (bottom) for selected temporal baselines (shown in Table 1). For reasons of visualization, the interferograms are combined with a hillshade representation retrieved from the SRTM data. The extent is shown in Figure A1. This figure shows the modified Copernicus data.

such narrow perpendicular baselines are therefore less sensitive to the topographical contribution of the phase φ_{topo} and more suitable for the derivation of surface displacements between two passes [40]. The term of the critical baseline B_c was introduced by Zebker and Villasenor [46] as the upper limit of the perpendicular baseline above which the phase becomes completely decorrelated. It is dependent on the wavelength λ, the range distance R, the incidence angle θ, the inclination of the slope α, and the range resolution R_y and computed as shown in equation 5 (valid for flat terrains):

$$B_c = -\frac{\lambda}{2} \cdot \frac{R}{R_y \cdot \cos^2(\theta - \alpha)}. \quad (5)$$

For Sentinel-1 (incidence angles between 29° and 46°), the critical baseline roughly ranges between approximately 5 and 10 km. Accordingly, it is not a limiting factor for topographic mapping under the acquisition geometries defined for S1A and S1B. This is also supported by the performance report, which denotes the maximum loss of coherence due to the length of the perpendicular baseline below 5% [85]. However, perpendicular baselines below 50 m are a problem for the retrieval of DEMs from Sentinel-1. It should be mentioned in this context that other C-band constellations employed significantly larger perpendicular baselines: ERS-1/ERS-2: 75–400 m [71,86–89]; ERS/ENVISAT: 1,650–2,050 m [72,90–93]; and Radarsat: 100–1,400 m [94,95], and also that the TerraSAR-X/TanDEM-X constellation allowed perpendicular baselines of up to 4 km [32,96].

The role of the perpendicular baseline for Sentinel-1 InSAR applications is illustrated in Figure 7. As also indicated by equation 4, the height difference is represented by one phase cycle increases with smaller perpendicular baselines. Accordingly, short baseline image pairs are less sensitive to elevation differences. The consequences on the quality of the derived DEM are displayed in the row at the bottom of Figure 7, which clearly indicates the loss of elevation information for smaller perpendicular baselines and the increasing amount of phase noise. This is also indicated by the drastically increasing RMSEs

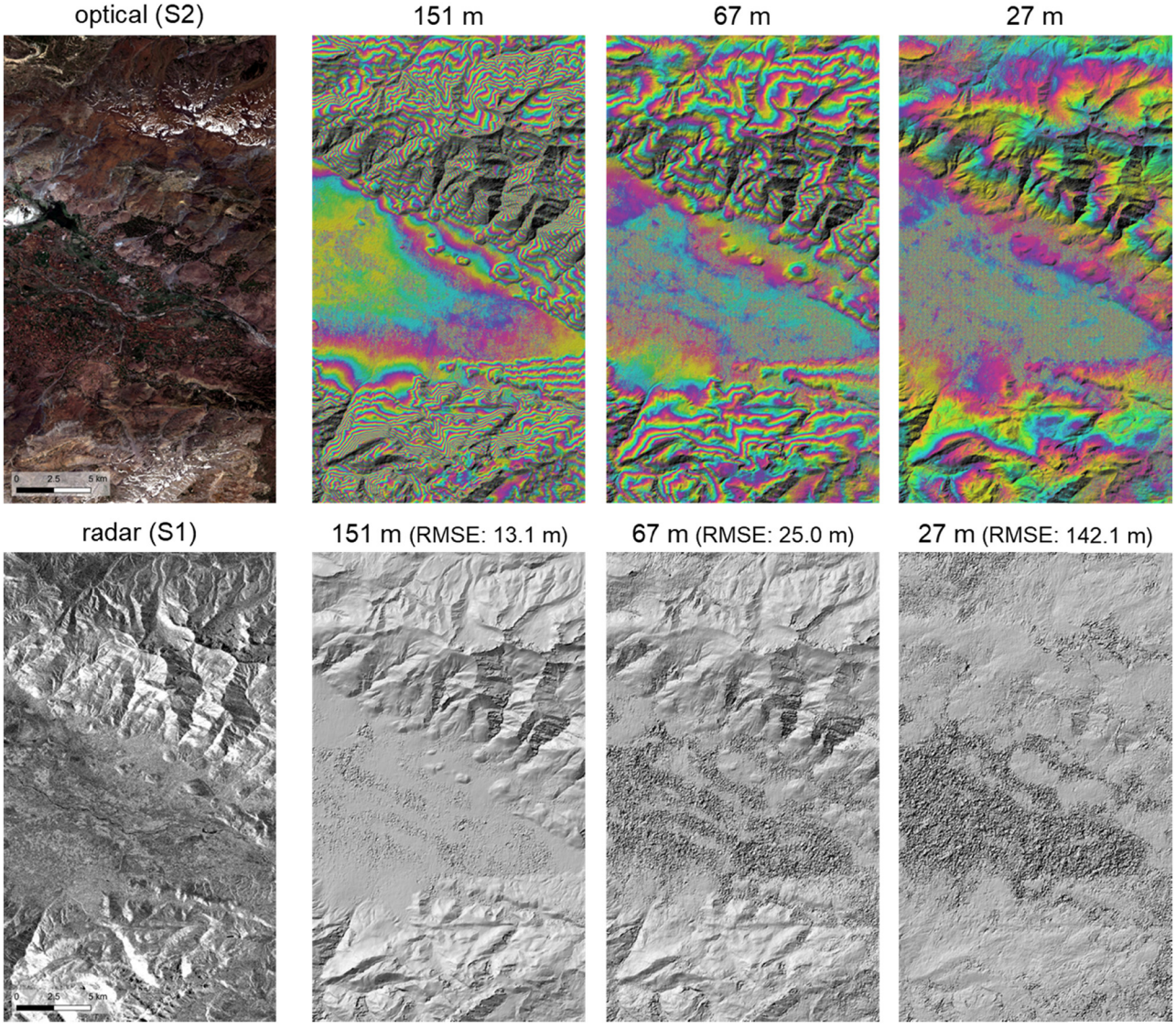

Figure 7: Interferograms (top) and hillshades of the derived DEMs (bottom) for selected perpendicular baselines (shown in Table 1). For reasons of visualization, the interferograms are combined with a hillshade representation retrieved from SRTM data. The extent is shown in Figure A1. This figure shows the modified Copernicus data.

of the derived elevations, which were calculated in comparison with the available SRTM heights.

2.1.5 Impact of other factors

Besides the temporal and perpendicular baselines, which are largely a matter of the selection of suitable images, there are geometric and topographic factors at the landscape scale, which also have an obvious impact on the quality of InSAR measurements. To demonstrate these effects, two profile lines were drawn across the study area as shown in Figure A1 (Supplementary data), one in azimuth direction across the valley (profile A, 40 km) and one in the range direction across the slopes of the *Esence* mountains in the north (profile B, 30 km). Elevations of the S1 DEM were extracted and analyzed for their differences to the reference SRTM heights. As shown by cross profile A (Figure 8, top left), there is a systematic overestimation of the overall elevation in the more level terrain (blue), while there is an underestimation of the heights of the mountain ridges (red). This is a typical sign for unwrapping errors accumulating across the image, slopes are especially underestimated then due to noise [97] and foreshortening [41]. A similar effect was reported by Singh et al. who created a DEM from ERS tandem pairs

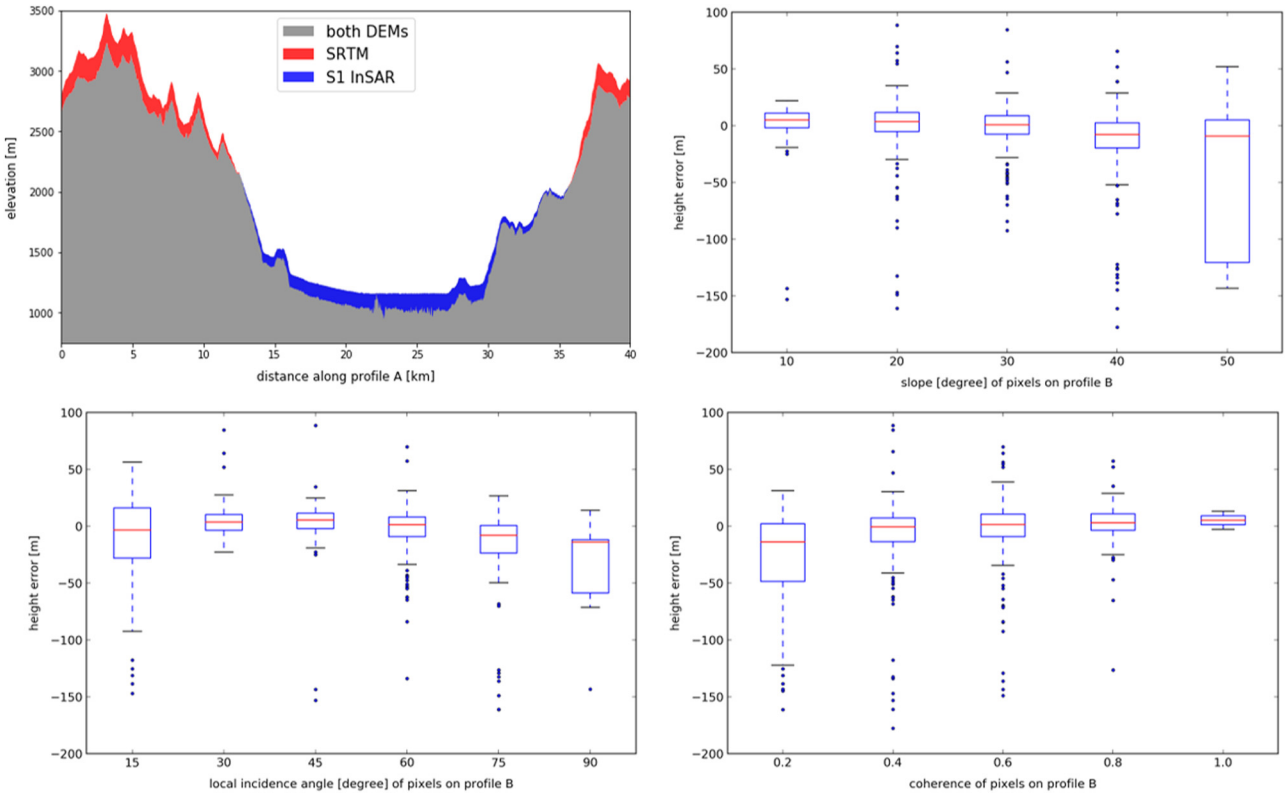

Figure 8: Impact of selected parameters on the height error (compared with SRTM). Top left: SRTM heights (red) vs S1 DEM heights (blue) along profile A (shown in Figure A1); top right to bottom left: height error in relation to coherence, local incidence angle, and slope for the pixels along profile B (shown in Figure A1).

(temporal baseline of one day) for parts of the Swiss Alps and also observed that the underestimation of slopes led to a "smoothened" topography in comparison with a higher resolution reference DEM [98].

Another reason can be orbital ramps, which are introduced by inaccurate coregistration and insufficient quality of orbit information [23,99]. One way to deal with these kinds of systematic errors is to model the overall spatial phase trend in the data by linear regression or polynomial approximation and remove it from the data before [86] or after unwrapping [43]. The impact of orbital errors on Sentinel-1 interferometry is comparably small because of the provision of precise orbit information [81] and high coregistration accuracy achieved through enhanced spectral diversity (ESD) coregistration, which corrects for the azimuth-dependent Doppler variation within the bursts [100]. Even if Sentinel-1 data can be processed with very high accuracies, already small azimuth offsets of a few centimeters can produce a phase ramp in the azimuth direction [101,102]. Together with the aforementioned slope underestimation, this explains most of the differences between SRTM and S1 elevations as observed along with profile A (Figure 8, top left).

But there are also effects in the range direction, which are discussed briefly in the following. It was already denoted in the study by Madsen et al. that height errors are strongly correlated with terrain modulation, especially with steep slopes [23]. Accordingly, the steepness of slopes is not only potentially underestimated over the entire image as mentioned earlier but also can lead to local height errors in extreme terrain. This effect is visible in Figure 8 (top right), where height errors are compared for all pixels along profile B in an aggregated form. The box plot shows that height errors, as the difference between the SRTM, are comparably small over slopes between 0 and 40°, but drastically increase for slopes above this value. The plot shows that underestimations of up to 150 m occur at all pixels along the profile, but with significantly higher interquartile ranges for slopes above 40°. Accordingly, in the investigated case study, the overall elevation estimates are good, but predominantly inaccurate for local extremes. This relationship between slope gradient and height errors was systematically analyzed and proven by Zhang et al. who compared a DEM derived from ENVISAT interferometry with the near-globally available SRTM [103].

To put these findings into another perspective, the second plot (Figure 8, bottom left) shows the height error in relation to the local incidence angle. This variable is different from the overall slope because it takes into consideration both the looking geometry of the sensor and the alignment of the landforms with respect to the flight direction of the satellite. As a consequence of the side-looking acquisition principle of spaceborne SAR sensors, geometric distortions occur in the image, often summarized as foreshortening, layover, and shadow [104]. Reasonably, these not only affect the retrieval of backscatter intensity but also result in errors in interferometric approaches, such as presented by Eineder and Holzner who demonstrate systematic effects for InSAR DEMs in areas of radar shadow [105]. In addition, Singh et al. and Breidenbach et al. report larger error rates for InSAR height estimates in areas facing away from the sensor [98,106]. This effect is also shown in the box plot, which confirms larger relative height errors for pixels with incidence angles below 30° and above 75°. The "optimal incidence angle for SAR images over alpine terrain" [105] of 45° shows the lowest error rates, furthermore underlining the local sensitivity of InSAR DEMs toward terrain aspects with respect to the satellite's position. While the shadow areas are simply voids in the retrieved radar image, they cause phase jumps during the unwrapping, which, when untreated, cause false elevation estimates [22]. Different approaches are presented to overcome these voids in the phase image by finding optimum unwrapping paths [60], for example, by using coherence as a measure to connect the surrounding unwrapping paths [107], by restoring the phase in shadow areas using smooth phase gradients [108], or by the combination of interferograms of multiple looking directions and aspects [109,110].

Finally, sufficiently high coherence is required for accurate height estimates, which can strongly vary over the entire image. For instance, decorrelation can occur through variations in land cover and scattering mechanisms as discussed in Section 2.1.3, but also results from the aforementioned shadow or layover effects [97]. An extensive analysis of terrain effects on DEMs retrieved from ERS data is provided by Zebker et al. [111]. Unsurprisingly, InSAR height errors primarily occur in pixels with coherence smaller than 0.2 and continually decrease with higher coherence in our study as well (Figure 8, bottom right).

Another important source of error are atmospheric effects. Although the retrieved backscatter intensity of radar sensors is significantly less affected than the optical data, heterogenous refractivity distributions in the atmosphere can cause an inconsistent signal delay within an image [24]. This was already investigated by Goldstein in 1995 who identified patterns in an interferogram, which were not correlated with topographic features and could therefore be attributed to water vapor and turbulence in the troposphere [75]. However, their impact becomes visibly more obvious in DInSAR approaches where the topographic phase φ_{topo} is already removed [112]. Especially time-series approaches based on many interferograms allow to systematically screen for atmospheric effects that can then be subtracted from the analysis [47]. As removing the topographic phase is not possible within the scope of DEM generation, its contribution has to be assumed negligible [27] or targeted by more advanced methods, such as weather models, data fusion, or multi-baseline approaches [57,113–115].

Luckily, the unknown delay of tropospheric effects is independent of the wavelength, but inversely proportional to the length of the perpendicular baseline, so that it is minimized for configurations above 100 m as suggested in Section 2.1.4 [116]. However, the radar signal also undergoes a phase advance in the ionospheric layer of the atmosphere, leading to additional distortion, especially in the mid-latitudes [117]. Its effect on C-band Sentinel-1 data is lower than for long-wavelength systems, such as ALOS-2 (0.034 vs 0.13 ionospheric induced phase [118]), but especially for DInSAR approaches, it should not be neglected, where Gomba et al. propose a split spectrum–based approach for Sentinel-1 TOPS data [119].

2.2 Open software, tools, and tutorials

Of all the existing spaceborne SAR missions, Sentinel-1 stood out since the beginning because its data were made openly available to the public via the Copernicus Open Access Hub [120]. Although the data of historic missions, such as ERS or ENVISAT, become progressively released as well [121], it was a constituted aim of the Copernicus Programme to provide unrestricted access to every citizen throughout the world and to foster science, economic growth, and decision-making the European Union [122]. Since then, the annual amount of data provided and downloaded by users is continuously growing: in the year 2019, over 128 million downloads (70 PiB) were registered, which is double the amount of 2018 and 20 times the volume of 2015 [123]. The operation acquisition of the Earth's surface is clearly defined in observation scenarios, which aim at exploitations of the S1 duty cycle and allowing users to integrate future acquisitions in their planning [38]. Until June 2020, each land surface

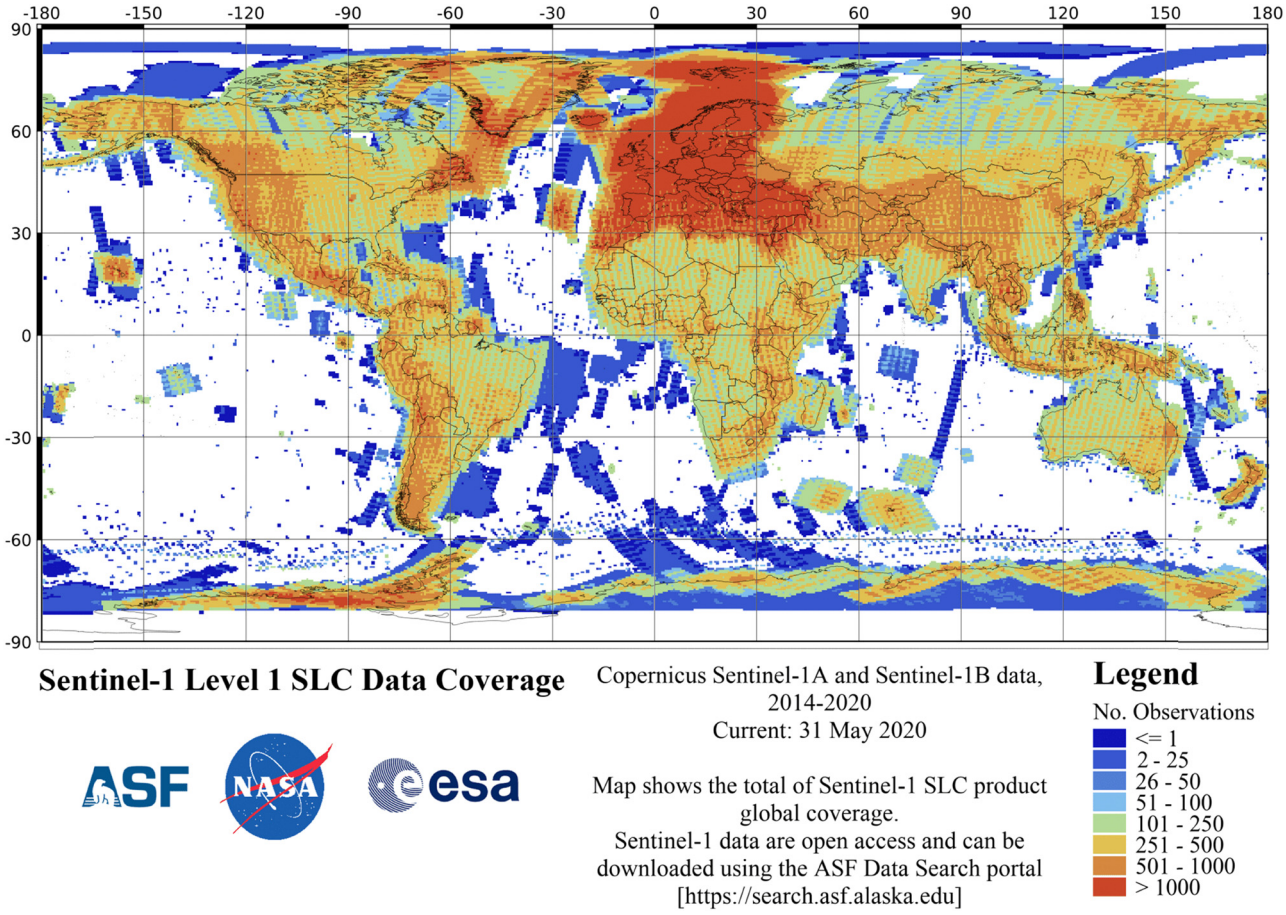

Figure 9: Global coverage of Sentinel-1 SLC products as of May 2020. Obtained from https://asf.alaska.edu and kindly provided by the Alaska Satellite Facility [198].

of the Earth was captured hundreds of times, with regional differences as shown in Figure 9. It shows the priority of the European Union and its surrounding seas, selected islands, and Greenland for the monitoring of sea-ice and iceberg monitoring as defined in the Sentinel High-Level Operations Plan (HLOP [124]).

Besides the actual open availability of data from the Copernicus Open Access Hub [120], the SNAP software [125] is continuously being developed by the order of ESA to assist all users in the exploitation of the products provided within the Copernicus Programme. By the end of 2019, it was downloaded over 500,000 times [126], making it the most actively used open-source software in the domain of remote sensing. It not only allows basic operations of SAR preprocessing and analysis but also provides all necessary tools to generate DEMs from nearly all spaceborne sensors, which are currently accessible by the public. A workflow on the derivation of DEMs from Sentinel-1 SLC image pairs is demonstrated in Figure 10 for a study site shown in the Appendix (Figure A1). The basic steps include TOPS Split, which reduces the SLC data to one sub-swath and a selected number of bursts [102], then coregistration by Back Geocoding and ESD [100], and interferogram formation (including removal of the flat-Earth phase φ_{flat}). The phase unwrapping is conducted outside SNAP by independently licensed tool *snaphu* (statistical-cost network-flow algorithm for phase unwrapping [127]) followed by the import of the unwrapped phase back into SNAP where it is translated into metric units based on an external reference DEM [66] and geocoded using Range Doppler terrain correction [68]. A tutorial on this process has been provided, including a number of potential error sources and limitations as discussed in this study [128].

A python-based implementation of these steps is also facilitated within the openly available tool GITASAR [129]. There are a number of additional open packages for radar processing, but these focus on polarimetry (PolSARpro-BIO [130]; OTB [131]), differential interferometry (ISCE [132]; LiCSBAS [133]; StaMPS [134]), or the exploitation of large data cubes (pyroSAR [135], OpenDataCube [136]) and do not include DEM generation in particular.

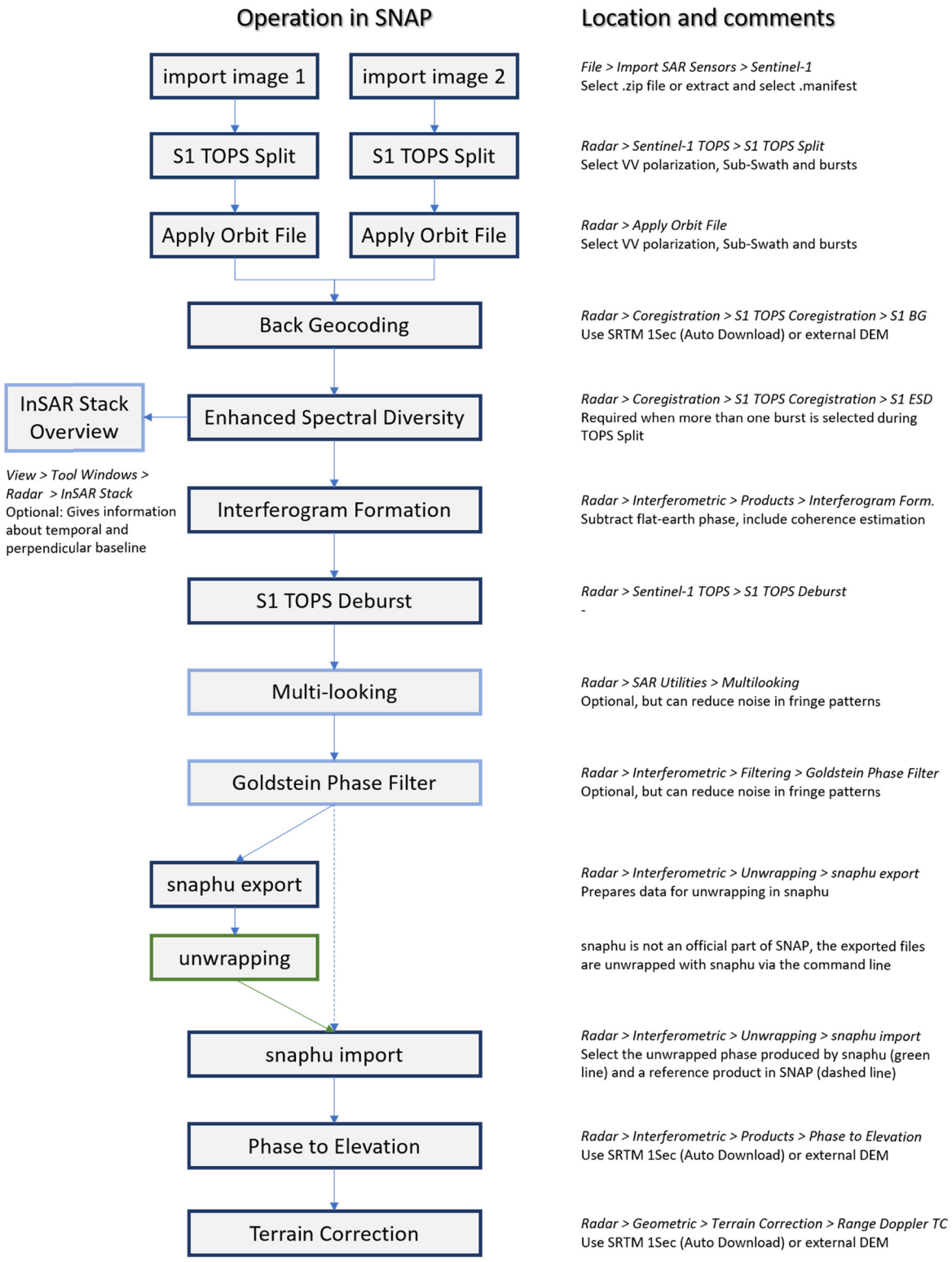

Figure 10: Workflow for the DEM generation from Sentinel-1 SLC data in SNAP. Optional operators are outlined in light blue, and external modules are marked green.

Besides the already mentioned tutorial provided by ESA [128], which is currently the most comprehensive, there are further open resources on DEM generation with Sentinel-1 data: the ASF provides a short, but technically complete list of instructions for the processing of an S1 InSAR DEM in SNAP [137]. It briefly discusses the

aspect of perpendicular baseline, but does not provide practical recommendations or further theoretical background information. Two tutorials on DEM generation using Matlab and Python (including scripts and sample data) are provided by the SAR-EDU initiative, but they are not based on Sentinel-1 products as input data, which are of the special structure due to the TOPS acquisition mode [138]. Geymen introduced the workflow of DEM generation with two ERS images and included the source code to execute it in the DORIS software package [139]. The article comes with a clear technical description, a thorough methodological discussion and includes relevant literature references for further reading. A similar approach was followed by Crosetto who described and discussed the processing chain to derive a DEM from ascending and descending ERS images with a focus on quality assessment and height calibration [57]. In a similar way, the mathematical foundations are well outlined and illustrated by many examples in a guide written by Richards, but also mainly without references to specific software packages or practical instructions [66]. Concludingly, the challenges to generate DEMs from InSAR image pairs are well discussed and presented in the scientific discourse but, except for the tutorial published by ESA [128], only a few openly available resources deal with the practical implications for the use of Sentinel-1 data.

3 State of research

3.1 Literature review

To get an impression about the current state of research, a systematic review was conducted to identify all articles published until October 2020 related to this topic. To cover the majority of peer-reviewed scientific contributions, *Web of Science* (WoS) was selected as a first source and searched according to the criteria given in Table 2. As a platform for the exchange of innovative concepts before peer-reviewed publication, *arXiv* was also searched for results. To find additional conference contributions or gray literature, Google Scholar was searched, which offers a broader, less scientific range of results. This allows the depiction of the status of current ideas and research beyond those of officially published works.

To include both adjectives (topographic) and nouns (topography) as wells as both singular (elevation) and plural (elevations) spellings, asterisks were used for the search. The results of the first survey are presented in Table 3. In total, 101 studies matched the criteria, of which the highest number was found in WoS (n = 52). However, only 14% of these met the criteria defined in Table 2. In contrast, the proportion of usable studies was 28% for Google Scholar and 17% for *arXiv*. The suitability of the studies was evaluated independently by two persons, initially screening the abstracts and then determining if the study fulfilled the criteria. Articles that were not published in English were translated by native speakers before the review. In cases where these two evaluators did not come to the same conclusions or

Table 3: Summary of the literature review

Portal	Results	Usable	Not usable
WoS	52	8	44
arXiv	6	1	5
Google Scholar	43	12	31
	101	**21**	**80**

Bold values are the sum of the lines.

Table 2: Criteria for the literature review

Data base	Web of Science (WoS), Google Scholar
Search terms	• Title: Sentinel-1 AND height • Sentinel-1 AND (Digital Elevation Model OR Digital Surface Model OR Digital Terrain Model) • Sentinel-1 AND (Interferometry OR InSAR) • Surface detection
Inclusion criteria	Articles, reports, and presentations (since 2013) dealing with • The extraction of elevations of terrain • The extraction of elevations of distinct surfaces • The extraction of heights of single objects from radar interferometry using Sentinel-1 data
Exclusion criteria	• Sentinel-1 was not used • Studies following a differential InSAR approach • Studies using Sentinel-1 for the estimation of vegetation heights based on statistical regression • Studies on ocean wave heights

Table 4: Summary of studies on elevation extraction from Sentinel-1 data

Authors (alphabetic order)	Type of publication (peer-reviewed), pages	Aim, location and extent	Value range	Number of images	Perpendicular baseline	Temporal baseline (days)	Validation data	Validation measures
Ahmadabadi et al. (2020) [159]	Journal article (yes), p. 17	Surface changes (dunes), Aredstan (Iran), 6 km^2	930–990 m	2	Not specified	12	110 GCPs	R^2: 0.73, MAE: 2.06 m RMSE: 2.42 m
Atalay and Sefercik (2018) [140]	Conference proceedings (no), p. 4	Topography, Zonguldak (Turkey), 350 km^2	0–540 m	2	Not specified	12	Local photogrammetric DSM (10 m)	StD: 4.2 m (flat), 5.2 m (entire area) NMAD: 3.7 m (flat), 4.0 m (entire area)
Dabiri et al. (2020) [156]	Journal article (yes), p. 20	Surface changes (landslide), Hítardalur valley (Iceland), 45 km^2	89–743 m	3 × 2	134/142/159 m	6	ArcticDEM (2 m)	RMSE: 30 m/37 m/46 m (vertical) MI: 0.92/0.97/0.97
Ghannadi et al. (2017) [143]	Conference proceedings (no), p. 4	Topography, Kavir desert (Iran), 400 km^2	1,555–2,080 m	2	Not specified	72	1 m reference DEM (not specified)	StD: 1.26 m (flat), 10.32 m (mountainous)
Ghannadi et al. (2019) [142]	Journal article (yes), p. 14	Topography, Kavir desert (Iran), 400 km^2	Not specified	2	Not specified	72	1 m reference DEM (not specified)	StD: 1.26 m (flat), 10.32 m (mountainous)
Ghannadi et al. (2020) [144]	Journal article (yes), p. 15	Topography, Tehran, and Jam (Iran), 7/10 km^2	0–220 m, and 579–830 m	2 × 2	Not specified	180/24	GeoEye-2 stereo image DEMs (1 m), validated for raw, median-filtered and 2D Kalman-filtered DEM	MAE (Tehran): 17.0/16.8/15.43 m RMSE: (Tehran): 24.3/23.1/20.1 m MAE (Jam): 16.0/15.7/14.8 m RMSE (Jam): 20.7/20.4/18.5 m
Kakavas et al. (2018) [149]	Journal article (yes), p. 14	Topography, Ksiromero (Greece), 150 km^2	0–220 m	8	Not specified	Not specified	38 GCPs	RMSE: 38.9 m Identification rate of karst features: 68.8%
Kumar and Krishna (2019) [153]	Journal article (yes), p. 6	Canopy surface heights, Tundi forest reserve (India), 75 km^2	9.5–23 m	2	90 m	12	11 tree height measurements	R^2: 0.889, MAE: 1.3 m, RMSE: 1.34
Kyriou and Nikolakopoulos (2018) [157]	Journal article (yes), p. 10	Surface changes (landslide), Moira (Greece), 1 km^2	720–810 m	2 × 15	96–170 m	12	None	None
Letsios et al. (2019) [155]	Conference proceedings (no), p. 4	Building heights, Larisa (Greece), 20 km^2	11–324 m	6	114–171 m	6/6/24/36/48	35 GPS measurements from rooftops	MAE: 1.64 m

Table 4: Continued

Authors (alphabetic order)	Type of publication (peer-reviewed), pages	Aim, location and extent	Value range	Number of images	Perpendicular baseline	Temporal baseline (days)	Validation data	Validation measures
Mohammadi et al. (2018) [145]	Journal article (yes), p. 6	Topography, Cameroon Highlands (Malaysia), 85 km^2	953–1,944 m	2	Not specified	602	AIRSAR DEM	R^2: 0.996, standard error: 1.99628 but results invalid
Nikolakopoulos and Kyriou (2015) [152]	Journal article (yes), p. 17	Topography, Mykonos/Lesbos (Greece), 86/1,650 km^2	0–395 m	21/25	175–1,050 m	12	A-GDEM/SRTM, Hellenic Cadastre DEM, topographic map; 19/>100 GCPs	RMSE (GCP Mykonos): 5–22 m, RMSE (GCP Mykonos): 10–85 m, but based on more GCPs
Nikolakopoulos et al. (2015) [146]	Conference proceedings (partly), p. 9	Topography, Mykonos (Greece), 86 km^2	0–395 m	Not specified	Not specified	Not specified	Hellenic Cadastre DEM, 19 GCPs	AD (DEM): –3.2 m AD (GCP): –19.5 m RMSE (GCP): 20.94 m
Nikolakopoulos et al. (2016) [158]	Conference proceedings (partly), p. 10	Topography, Panagopoula (Greece), 10 km^2	0–750 m	11	Not specified	Not specified	GCPs (number unknown)	AD (GCP): 9.12 m RMSE (GCP): 14.7 m
Nonaka et al. (2019) [150]	Conference proceedings (partly), p. 4	Topography, Tsukuba (Japan), 64 km^2	0–30 m	7	46–137 m	6	61 GCPs, coherence	RMSE: 6.3–31.0 (larger with smaller b_{perp})
Ortone Lois (2020) [154]	Conference presentation (no), p. 15	Surface height (glaciers), Videma/Frías (Argentina), 50 km^2	100–2,100 m	2 × 8	24–180 m	6–24	None	Not specified
Sefercik et al. (2018)	Journal article (yes), p. 15	Surface heights, Istanbul (Turkey), 100 km^2	20–320 m	2	86 m	6	Airborne laserscanning DEM (5 m)	StD: 5.6 m (entire area), StD: 5.1 m (flat) NMAD: 4.6 m (entire area) NMAD: 3.6 m (flat)
Soni et al. (2021) [147]	Book chapter (no), p. 10	Tonk district (India), 7,200 km^2	260–300 m	2	Not specified	12	None	Visual
Sunu et al. (2019) [148]	Journal article (yes), p. 10	Topography, Semarang (Indonesia), 375 km^2	0–460 m	2	146 m	18	137 GCPs	AD: 38.7 m RMSE: 52.3 m
Ullo et al. (2018) [151]	Conference proceedings (partly), p. 8	Topography, Ischia island (Italy), 46 km^2	0–750 m	8	7/32/55/108 m	6/6/12	Coherence	None
Yang et al. (2018) [160]	arXiv article (no), p. 5	Kavir desert (Iran), 400 km^2	Not specified	2	Not specified	6	Reference interferogram	rRMSE: 28.7 (10 m), 25.1 (25 m)

AD = average difference, GCPs = ground control points, MAE = mean absolute error, MI = Moran's I, NMAD = normalized mean absolute deviation, RMSE = root mean square error, R^2 = coefficient of determination, SE = standard error, StD = standard deviation.

were not sure about the suitability of the work, a third reviewer made the final decision. The reasons for dropping unsuitable papers were because the study was based on DInSAR (23.8%), the study focused on ocean heights (18.8%), object heights were retrieved by regression (37.5%), or other topics were covered containing the search terms within a different approach (37.5%).

3.2 Current studies on elevation extraction

3.2.1 Aims and data sources

As some studies were duplicate listings by both WoS and Google Scholar, the total number of papers relevant for this review was 21. A summary of all studies is given in Table 4. Most of these aim at the estimation of local or regional topography based on a pair of Sentinel-1 products, similar to the examples shown in Section 2. They are distributed over different continents, altitudes, and ecosystems: Northwestern Turkey [140,141], the Kavir Desert [142], and the cities of Tehran [143,144] and Jam [144] in Iran, the Cameron Highlands in Malaysia [145], the island of Mykonos, Greece [146], the Tonk district in India [147], and the municipality of Semarang, Indonesia [148]. To increase the quality of the elevation estimates, seven to eight images were used in studies on Ksiromero, Greece [149], Tsukuba, Japan [150], and the island of Ischia, Italy [151]. A study on the Greek islands of Mykonos and Lesbos takes a special role because 21 and 25 image products were combined to generate DEMs [152].

Three studies explicitly target the retrieval of surface heights of natural and man-made structures, which can be considered a special challenge because they are not part of the observed topography but rather have their own limited extent within the setting. These studies use different quantities of input images and deal with the estimation of canopy heights of the Tundi forest reserve, India [153] (n = 2), the surfaces of two glaciers (Videma and Frías) in Argentina [154] (n = 8 per glacier), and also building heights in the city of Larisa, Greece [155] (n = 6).

The third group of studies uses images of multiple dates to assess elevation changes related to geomorphologic processes. While this is usually done with differential interferometry (exclusion criterion for this review), three studies derived DSMs for pre and post landslide situations to calculate volume differences for the Hítardalur Valley, Iceland [156], and the landslides of Moira [157] and Panagopoula [158] in Greece. A fourth study investigated the movement of dunes around the city of Ardestan, Iran [159].

The study by Yang et al. [160] has a special role because of its experimental character. It does not aim at the construction of a DSM alone, but investigates if and how radar images of different pixel spacings can be combined to achieve a DSM at high spatial resolution. It was tested in the Kavir Desert in Iran based on o a 6 day image pair in a stripmap mode.

3.2.2 Methods and outcomes

This section presents the contents of the studies (Table 4) in greater detail and reflect their approaches with respect to the principles and aspects of InSAR elevation extraction as outlined in Section 2.1. This section summarizes the current efforts and shortcomings in DEM generation from Sentinel-1 data to stimulate joint discussions on how to shape this field in the future. To grant an objective view on these studies, emphasis will be placed on the impact of different parameters and the reported form of validation of results as major indicators for transparent and good scientific practice.

Articles that were published by the same authors are evaluated together to embrace them as parts of a larger research aim, which was split into different aspects.

Against this background, Nikolakopoulos and Kyriou were among the first to approach the potential of Sentinel-1 data for the mapping of topographic heights of the Greek islands of Mykonos [146] and Lesbos [152] in 2015, shortly after the launch of Sentinel-1 in late 2014. In both studies, their approach was based on a series of interferograms, which were systematically divided into two groups of small (nine image pairs [b_{perp}: 175–350 m]) and large (21 image pairs [b_{perp}: 175–1,225 m]) perpendicular baselines to analyze the effect of this parameter on the DEM quality for Mykonos. For the island of Lesbos, results gained from ascending (nine image pairs) and descending (14 image pairs) orbits were compared to analyze the impact of look direction on the final result. For both islands, image pairs of perpendicular baselines larger than 175 m (up to 1,225 m) are reported, so that all of them fulfill the quality criteria suggested by the scientific literature as outlined in Section 2.1.4. Neither the interferograms falls below the minimum baseline of 150 m nor exceeds the critical baseline of around 5 km. The actual method of combining elevations derived from the different pairs into a single result is not described in the studies, but it is referred to in a previous article by Choussiafis et al. [161], which proposes a form of mosaicking where elevation values at single pixels are combined based on weights derived from a height accuracy map,

which is produced along each DEM. This height accuracy map is computed based on an external reference DEM and allows the determination of the quality of a local height estimation. After selection of a threshold value, which was reported to lie around the vertical accuracy of the reference DEM, height pixels that exceed this threshold value are masked out and only pixels remaining from other interferograms are then used to compute a final height value weighted by coherence and baseline. The authors report that this method produces DEMs with significantly higher similarity to the reference DEM compared to the standard averaging methods. The authors' studies evaluated in this article are based on this method and reference it in their methods section; yet, short discussions on the principles underlying the mosaicking process would increase transparency and help readers understand how the DEMs were generated in each respective study. After computation of DEMs of the two islands, the studies propose various forms of validation: (a) visual comparison with reference DEMs, (b) statistical comparison with reference DEMs, and (c) the evaluation of the derived heights against measured ground control points (GCPs). Splitting the accuracy assessment into several parts is advisable because each of them addresses different aspects: visual comparison helps to evaluate the overall data quality and search for artifacts (e.g., generated during the unwrapping process) and systematic errors, such as underlying ramps or general trends (e.g., underestimation of high values, like demonstrated in Figure 8). This was done by comparing color-coded elevation maps and cross-profiles from the generated DEMs of Mykonos and Lesbos with reference DEMs. The authors used data of different spatial resolutions obtained from SRTM (30 m), ALOS PRISM (2.5 m), and the Hellenic Cadastre authority (5 m), and also DEMs derived from contour lines topographic maps (7.5 m). This allowed obtaining a more objective and scale-independent view of the results without being limited to only one reference dataset, although they conclude that in most cases, reference data of the highest resolution and the lowest vertical accuracy should be preferred. In a second step, descriptive statistics on the elevation values of the produced and reference DEMs are compared. This does not give detailed insights on the local accuracy of the results, but does enable checking if the DEMs fall within the same value ranges as the reference data (minimum and maximum) and for an overall offset of the values (median). For example, the S1 DEMs produced for both Mykonos and Lesbos have higher maximum values (392 and 970 m) compared to their reference datasets (360 and 940 m), indicating potential overestimation of the highest peaks. For a more robust analysis of these indications, GCPs of certified elevation were used for the computation of the RMSE as a more specific accuracy measure, which compares the difference of the produced DEM elevations to that measured at the GCPs. As shown in Table 4, depending on the reference DEM, the RMSE lies between 5 and 22 m for Mykonos and between 10 and 85 for Lesbos, but it has to be noted that the overall number of GCPs is not reported in the articles, but is considerably lower for Mykonos (~19) than for Lesbos (>100), based on a visual inspection of the presented GCP maps. As a second measure, the average difference (AD) was calculated for Mykonos between the S1 InSAR DEM as well as both the Hellenic Cadastre reference DEM (−3.2 m) and the available GCPs (−19.5 m). With respect to their study design, the studies found no difference in accuracy between the short and long perpendicular baseline groups of Sentinel-1 image pairs because both groups lie within the critical baseline of around 5 km. In addition, DEM mosaics computed from ascending and descending tracks led to similar accuracies, so that no benefit regarding the looking direction could be identified for this area as well.

In a later study, the authors applied the same methodology of mosaicking of Sentinel-1 derived elevations to characterize natural karst depressions in limestones of the Ionian geotectonic zone in Western Greece [149]. Besides the elevation model generated using eight Sentinel-1 products, openly available data of SRTM, ASTER GDEM, ALOS GDEM (all 30 m), and a DEM were generated from contour lines of a topographic map (20 m), as well an orthomosaic generated by photogrammetric processing of aerial images by the Hellenic Cadastre (5 m). Of all elevation products, the Sentinel-1 DEM showed the largest RMSE 38.9 m based on the elevation information of 38 GCPs collected in the field, which is high compared with the openly available DEMs (8–22 m) and the Hellenic Cadastre (2.4 m). In addition, the suitability of the Sentinel-1 DEM for the automated detection of karst features was determined with an identification rate of 69%, which lies above those of ALOS (66%) and the Greek Cadastre (22%), but below those of SRTM (73%) or the one derived from the topographic map (89%). The authors assume that the automated detection of karst features is sensitive to the scale of the input DEM, and therefore, products of higher resolution partly result in the lower quality. Yet, the DEM from Sentinel-1 data resulted in similar results as other freely available elevation products.

The method of mosaicking several Sentinel-1 DEMs was also applied by this group of authors to an area in the northern Peloponnese, which is reported as being

especially susceptible to landslides, and DSMs of different dates could be used for the estimation of surface changes [158]. This study does not analyze a special landslide event but can be seen as a preparatory work for the development of a monitoring strategy based on freely available InSAR data. Eleven Sentinel-1 products were used to generate a DEM as proposed by Choussiafis et al. [161], and outcomes were visually and statistically compared with a reference DEM of the Hellenic Cadastre (5 m), an unknown number of GCPs, and a DEM generated from a series of TerraSAR-X Spotlight products with a spatial resolution of 1 m. All three DEMs were statistically validated against the GCPs (but not against each other), reporting an AD of 9.1 m and an RMSE of 14.7 m for the Sentinel-1 DEM. The authors conclude that neither the Sentinel-1 nor TerraSAR-X DEMs provide the necessary accuracy to detect and measure small-scaled landslides in this area. This study was continued by Kyriou and Nikolakopoulos in 2018 [157] who undertook extensive surveys in the area with Global Navigation Satellite System (GNSS) measurements and flight campaigns of unmanned aerial vehicles (UAV) to measure topographic heights of the Moira landslide in January 2016 and had an extent of 300 m by 330 m. A total number of 30 interferograms were computed with perpendicular baselines between 97 and 172 m of which 15 describe the surface before the landslide event and 15 afterward. The study does not give information on how these 15 interferograms were merged to one final DSM. As the authors coincide with the previously presented studies, it is assumed that the same method of mosaicking was undertaken, but still, this is a drawback because it prevents reproducibility of the results. The elevation profiles of the pre-landslide and post-landslide DEMs were compared along three different transects, clearly showing a reduction of surface heights between 5 and 30 m, varying along the distance between the landslide crown at the top and the accumulation zone at the bottom. Unfortunately, thousands of GNSS measurements, which were collected along tracks in the study area after the landslide, were used only to estimate the volume of the displaced material by comparing them with the heights of the Hellenic Cadastre and not for the validation of the post-landslide DEM of Sentinel-1. Yet, the authors conclude from this assessment that the difference of surface heights retrieved by the two S1 DEMs are overestimated and do not provide a reliable estimation of the actual displacement.

The second group of articles by Ghannadi et al. who tested the interferometric capabilities of Sentinel-1 for different locations in Iran is presented later. Large parts of their study areas are characterized by sparse vegetation cover, so that the impact of temporal decorrelation is low compared to other studies. The first article targeted the derivation of surface topography around the city of Tehran based on a single image pair with a temporal baseline of 72 days [142,143]. No information is given on the perpendicular baseline, but the large distance of the fringes in the interferogram presented in this study indicates a baseline smaller than 100 m (comparable to that of the shortest perpendicular baseline shown in Figure 7). The results were validated against two sets of height reference points extracted from a DEM with a spatial resolution of 1 m (source not specified): the standard deviations (StDs) between both datasets were 1.26 m (flat areas, based on 138,761 reference points) and 10.32 m (mountainous areas, based on 78,196 reference points), with large proportions of errors smaller than 10 m, but outliers reaching up to 20 m.

To tackle these outliers more effectively, the findings of Ghannadi et al. were refined in another study in Iran [144]. It uses two image pairs of different regions around the cities of Tehran and Jam with temporal baselines of 180 and 24 days, respectively. It is not justified in the article why these image pairs were selected, yet perpendicular baselines are not presented. The approach of the study is of rather experimental nature and analyzed how DEM accuracies change after the application of a median filter and a two-dimensional Kalman filter [162]. They also used a reference DEM generated by photogrammetric processing of GeoEye-2 image products with a spatial resolution of 1 m and a vertical accuracy of 0.5 m. Presumably, the same reference DEM was used in the studies mentioned earlier as well although its accuracy is not evaluated at a greater detail. Findings of both regions show that the RMSE of 24.3 m (Tehran) and 20.7 m (Jam) can be reduced slightly by the median filters (23.1 m and 20.4 m, respectively) and even more so by the proposed 2D Kalman filter (20.1 m and 18.5 m, respectively). The same is reported for the mean absolute error (MAE), which also slightly decreases after postprocessing. However, the authors conclude that the effect of filtering on the DEM quality is mostly limited to outliers, and it can be assumed that image pairs with more suitable temporal baselines (6–12 days) and larger perpendicular baselines can provide DEMs with lower error rates in general.

A similar study design has been presented by Atalay and Sefercik who estimate topography based on a single pair of Sentinel-1 images with a temporal baseline of 12 days in Zonguldak in Turkey [140] and validate the results based on a reference DSM with a spatial resolution of 10 m provided by local authorities. They performed a co-registration of the elevation models to minimize

systematic errors between both datasets to correct for horizontal shifts. This step resulted in horizontal shifts of 39.4 m and −23.8 m in x and y directions, which were corrected before the accuracy assessment. Afterward, they compared the StD and the normalized median absolute deviation (NMAD) between the reference DEM and the S1 DEM. The calculated StD was 4.2 m on the flat terrain and 5.2 m for the entire area. To put these values into perspective, StD was also assessed between the reference DEM and the AW3D30 model, attributing similar error rates (StDs of 4.0 and 5.5 m). The calculated NMAD was 3.8 m (flat) and 4.0 m (entire area) for Sentinel-1, and 3.2 m (flat) and 4.7 m (entire area) for AW3D30. Finally, the morphologic quality of the DSMs was assessed by visual comparison of color-coded contour levels. The authors conclude that Sentinel-1 data can deliver DEMs of similar quality compared to AW3D30, but the latter is more precise on flat terrain in the study area.

The comparison of DSMs from SRTM, AW3D30, and a Sentinel-1 image pair (b_{temp} = 12 days, b_{perp} = 86 m) was extended by Sefercik et al. for the metropolitan area of Istanbul [141]. A reference DSM with a spatial resolution of 5 m was used to calculate StD and NMAD of the height difference for different surface types. The study showed that StD of Sentinel-1 (5.6 m) is lower than that of SRTM (6.2 m) and AW3D30 (6.3 m) over the entire area (water bodies excluded), but especially AW3D30 performs better on flat terrain (4.9 m). With respect to different types of land cover, open areas were found to have the lowest NMAD (3.5 m), followed by forest (4.3 m) and built-up areas (3.8 m) for the Sentinel-1 DSM. Additional height error maps, contour lines, and cross sections were presented to illustrate the differences between the datasets. Especially the profile cross sections showed that some heights of building blocks were visible in the AW3D30 because it derived from a product with initially 5 m spatial resolution, while SRTM and Sentinel-1 were of comparably poor quality over the urban area.

Ahmadabadi et al. used a Sentinel-1 image pair separated by 12 days and a perpendicular baseline of 77 m to create a DEM of dunes near the city of Ardestan in the Iranian desert. It was validated against 110 GCPs with height information and achieved an overall agreement of R^2 = 0.73, an RMSE of 2.42 m, and an MAE of 2.1 m. They used it to estimate the direction and the horizontal movement of sand dunes based on a reference DEM and additional Sentinel-2 data, which were in line with the wind directions of a nearby meteorologic station. The detected horizontal displacements of the dunes showed an RMSE of 4.7 m and were found to be more frequent with increasing elevation, although this could also be attributed to a computational bias. The authors conclude that the looking direction of the satellites should be taken into consideration for future studies to increase accuracy.

In contrast to the sparsely vegetated areas, which were presented in the previous studies, Mohammadi et al. present a study based on an image pair of the Cameroon Highlands in Malaysia. which is characterized by dense forests, farmlands. and orchards and altitude differences of more than 1,000 m [145]. These challenging conditions, combined with a very large temporal baseline of 602 days, led to an entirely decorrelated interferogram without any fringe patterns as shown in the figures of the article. The unwrapped phase is therefore characterized by a strong ramp in the azimuth direction superimposing any topographically induced phase variations. As indicated by the graphical workflow, the topographic phase removal was applied to the data, and hence, the topographic phase estimation based on the SRTM data was then wrongfully interpreted as the actual output DEM. Accordingly, the accuracy assessment led to a coefficient of determination R^2 of 0.996 and a standard error of 1.9 m, which was basically just the SRTM data validated against itself at a resampled spatial resolution of 10 m. The authors conclude that the method was highly effective, but based on the presented data sources and the outlined workflow, the results clearly underlie false conclusions and were based on technically incorrect processing.

A short study was presented by Soni et al. who used a 12-day image pair to derive elevations in the district of Tonk, India [147]. No information on the perpendicular baseline is given, and the quality of the resulting DEM was only visually validated and discussed based on the coherence layer, which was reported low for croplands and water bodies. The authors suggest addressing this issue by combining images of S1A and S1B to reduce the temporal baseline to 6 days.

While the previously evaluated studies did not present or discuss the role of perpendicular baseline, all the following studies placed more emphasis on the selection of suitable image pairs with favorable configurations. Sunu et al. found an image pair separated by 18 days but with a perpendicular baseline of 146 m, which comes close to the ideal value range suggested in the previous studies mentioned in Section 2.1.4. Their study area is the region around Semarang, the capital of Central Java province in Indonesia. Altitudes roughly range between 0 and 500 m, and large parts of the study area are covered by swampy forests and cultivations. Therefore, the fringes in the interferogram are visible, but are interrupted by low coherence areas at several points. Their phase information could not be unwrapped correctly leading to artifacts in

the final DEM. Validated against 137 GCPs with elevation information, the AD was 38.7 m and reached values up to 206 m. Also, the RMSE of 52.3 m is comparably high, and according to the authors, the largest errors are concentrated in swamp areas and dense vegetation, while the AD was lowest over urban areas.

Similar challenges were reported by Ullo et al. who generated a DEM of the island of Ischia, Italy, in the context of an earthquake event, which was also assessed by differential interferometry (DInSAR). Hence, they used four different image pairs of varying look directions (ascending and descending), temporal baselines (6–12 days), and perpendicular baselines (between 7 and 108 m). They carefully discuss the potential impact of different error sources (atmospheric noise, temporal decorrelation, look angle, and surface orientation) and also underlining that pairs with the largest perpendicular baseline and highest coherence should bring the most promising results for topographic mapping. The resulting DEM contained smaller errors in the areas of dense forests, but according to the authors, the overall elevation patterns and value ranges were in accordance with those official topographic maps. No statistical evaluation based on independent reference data has been carried out for the generated DEM. Similar to the study by Mohammadi et al. [145], the information content of the topographic phase, which was estimated for the estimation of displacement of the study, was partly misinterpreted within the scope of DEM generation.

To study the impacts of the perpendicular baseline on DEM generation, Nonaka et al. analyzed six interferograms of Sentinel-1 image pairs of the city of Tsukuba, Japan [150]. Perpendicular baselines ranged between 46 and 137 m with temporal baselines between 6 and 24 days. They derived the height ambiguities for these pairs according to equation 4a and confirmed that larger height ambiguities caused by shorter perpendicular baselines lead to lower DEM accuracies. These were assessed by using a quantity of 61 height reference points and were reported the lowest (RMSE of 6.3 to 7.7 m) for the pairs with perpendicular baselines larger than 100 m and reached 31 m for the pair with 72 m and 24 days. The study furthermore showed that errors were larger for reference points collected over parking lots and roads than those from other ground surfaces. As the temporal baselines were not constant through the image pairs, the interpretability of the results is limited.

While the previous study intentionally limited the GCPs to ground surfaces, Letsios et al. tested the capabilities of Sentinel-1 interferometry for building height estimations in Larisa, Greece [155]. Six image pairs with temporal baselines between 6 and 28 days and perpendicular baselines between 114–171 m were used to generate individual DSMs, which were stacked and averaged in a second step to form a final urban DSM. Validation was based on 35 elevation measures collected at rooftops to obtain the topographic height including the surface of the building objects. Absolute errors ranged between 0.01 and 4.2 m and resulted in a mean average error (MAE) of 1.69 m. The authors conclude that the results can be useful at the block level, but the spatial resolution of Sentinel-1 is not sufficient to reliably predict single building heights. Also, the difference between the ground height and the object height is not assessed in this study.

Kumar and Krishna also investigated the interferometric potential for the retrieval of canopy heights of the Tundi forest reserve (India) comparing image pairs from Radarsat-1 and Sentinel-1. Their comparability was limited because of the different polarization (HH and VV), direction (ascending and descending), temporal baseline (24 and 12 days), and perpendicular baseline (491 and 90 m). After interferometric retrieval of surface heights, including the forest canopy, ground heights have been assigned to each forest area based on the nearest available vegetation gap to derive the local height of each forest stand. Different accuracy measures were calculated based on 11 height measurements collected in the field, each consisting of an average of 25 trees: R^2 between measured and predicted tree height was found to be 0.89 for both sensors, and RMSE (1.3 m) and MAE (1.34) were slightly lower for the Sentinel-1 canopy model, despite visually reported noise within dense forest areas caused by phase decorrelation. These low measures must be interpreted with care because of the low number of reference points (n = 11) and the long time between the Radarsat-1 DSM from 2004 and the Sentinel-1 DSM from 2017 which includes an expected height increase of around 4 m according to the authors. This is underlined by a comparably low R^2 between both DSMs of only 0.48. Still, the use of forest gaps to determine the difference between ground and surface heights was proven to be effective in this study and expected to be more efficient when more image pairs were combined.

A study on glacier heights in contrast to terrain heights was proposed by Ortone Lois for two glaciers in the Los Glaciares National Park in Argentina, with altitude differences of over 2,000 m [154]. Four Sentinel-1 image pairs of different years were used for each of them, with temporal baselines between 6 and 24 days and perpendicular baselines between 24 and 180 m. No statistical accuracy assessment was conducted, but the

impact of rainfall events on the phase information as well as the loss of coherence with the increasing temporal baseline was presented in the study. The quality of results was furthermore assessed by visual inspection of hillshade representations of Sentinel-1 DSMs compared to the SRTM data. The author concludes that the impact of vegetation, steep slopes, and moving ice masses was severely degrading the phase quality, and pairs with perpendicular baselines below 70 m were not usable in this case.

An approach comparing DSMs of three different acquisition periods was pursued by Dabiri et al. who used 6 day image pairs at perpendicular baselines between 110 and 159 m to assess the volume changes of a landslide in the Hítardalur Valley, Iceland [156]. As this event exceeded the maximum detectable displacement (half the size of the wavelength) and included non-coherent surface changes, a DInSAR approach was no longer applicable [24]. After masking the landslide area, volumes of 7, 12, and 109 million m³ were estimated by the three different post-event DSMs. To put these large variations into perspective, the ArcticDEM (2 m) [163] was used to validate the DEM areas outside the landslide event. Besides a statistical comparison, the vertical accuracy of the three post-landslide DSMs was assessed by the RMSE, while their horizontal accuracy was tested for autocorrelation by Moran's I index. It was applied to the difference image between the S1 DSM and the ArcticDEM and tests for local homogeneity within a kernel of eight neighboring pixels [164]. Results show that the DEM calculated from the ascending data with a perpendicular baseline of 134 m has the lowest RMSE (30 m compared to 37 and 41 m), but the DEM with a perpendicular baseline of 142 m produced the best volume estimation (7 million cubic meters, also confirmed by independent literature [165]), and has the highest Moran's I (0.97). The authors conclude that besides the factor of the perpendicular baseline, which has been carefully selected in the study, temporal decorrelation and weather conditions have a significant impact on the quality of the results, and therefore, the suitability of Sentinel-1 for landslide volume estimation has to be further investigated.

The last study presented in this work by Yang et al. is of an experimental nature and tested the hypothesis regarding if Sentinel-1 products could be combined with images of higher resolution to generate interferograms with higher details for DEM generation [160]. Their test was based on an image pair acquired in a stripmap mode (5 m spatial resolution) with a temporal baseline of 6 days acquired over the Kavir Desert in Iran, of which one was downsampled to 10 and 25 m for testing reasons. In a second step, an interferogram was computed using a compressive sensing approach developed by the author based on the product of high resolution (5 m) and each of the lower resolution images (10 and 25 m). The filtered and unwrapped phases were then compared to the high-

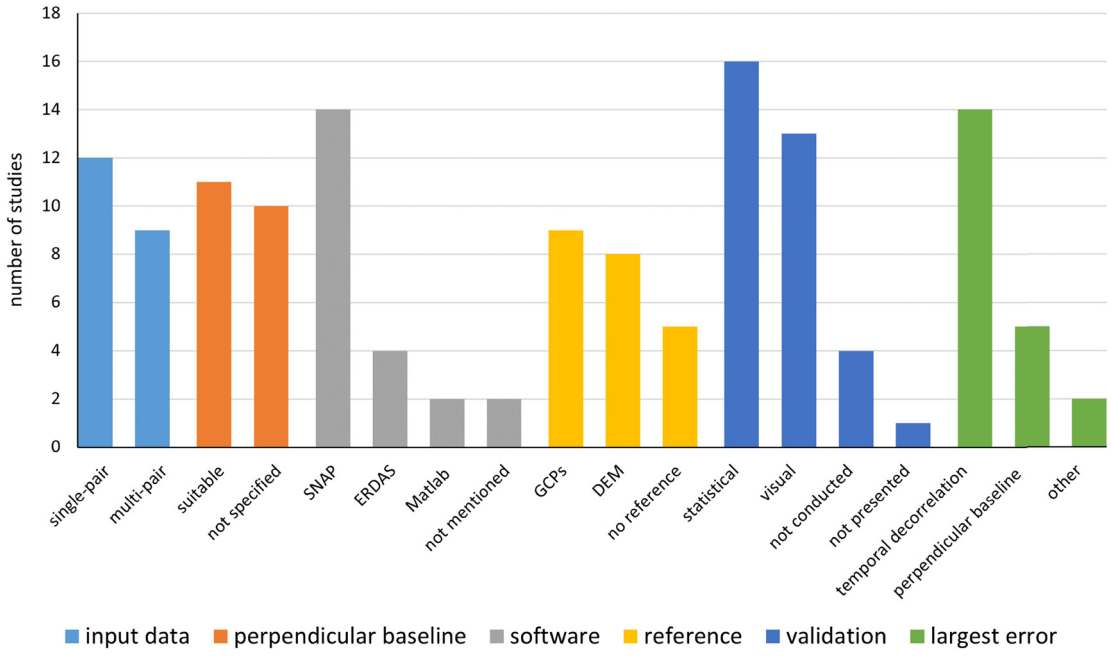

Figure 11: Overview of the study area. Extents and profiles used for demonstration in Section 2.1. This figure shows the modified Copernicus data.

resolution outcome by the relative RMSE, resulting in a relative phase difference of –28.7 (10 m) and –25.1 (25 m). No conversion to metric elevations was carried out, but the authors conclude that this method is suitable to increase the spatial resolution and degree of detail of interferograms. Yet, it remains unclear why the relative RMSE used for the quality assessment is negative and given in the decibel unit. Accordingly, generating interferograms from both stripmap and TOPS products should be further investigated.

Figure 11 presents a short summary of the literature review: around one half of the 21 analyzed studies dealt with the analysis of a single image pair, while the others used more advanced approaches. Most of the studies underlined the importance of short temporal baselines, but only half of them explicitly worked with pairs of suitable perpendicular baseline. It is unclear if the others simply did not mention this parameter or if they were not aware of its impact. Sixty-eight percent of all studies used SNAP for the data processing, which is not surprising, because it is the main software provided by ESA when making use of their satellite constellations. Besides this, ERDAS and Matlab were used as commercial alternatives. Half of all studies used field measurements of heights to validate their DSMs, which is considered the most precise validation, but collecting such data is time consuming, and many studies only used less than 50 GCPs for the calculation of specific error measures. Accordingly, these points were not necessarily representative of the entire study area. In cases where the field data were not available, validation has been conducted based on a reference DEM of higher resolution. This approach allows a considerably larger number of values for statistical comparison, but the accuracy metrics can be biased by the quality of the reference DEM. An advantage of this approach is that it allows the identification of the spatial distribution of errors, for instance, in relation to different types of land cover or with respect to topographic characteristics (e.g., larger errors at slopes). Based on either point-wise measurements or a reference DEM, most studies were able to conduct a statistical accuracy assessment. RMSE and MAE were the most popular measures because they are resolved in the same unit as the investigated DEM (m), but also the coefficient of determination R^2 was frequently used to quantify the overall agreement. Only few studies distinctively separated horizontal and vertical accuracy or checked for spatial autocorrelation with Moran's I. Finally, the main reported reason for low quality was temporal decorrelation, causing noise in interferograms because of low coherence. But it is obvious that some studies were not fully exploiting the potential range of the imaging geometry by selecting pairs with higher perpendicular baselines.

3.3 Experiences from the user perspective

This section is not based on published research, but shall give insights into the current debates, approaches, and problems of the user community of Sentinel-1 data. With over 7,100 users, 4,000–6,000 daily page views at average and 150–400 monthly posts, the user forum of the Scientific Toolbox Exploitation Platform (STEP) [166] hosted by the European Space Agency is considered a representative snapshot. In particular, the challenges of DEM generation with Sentinel-1 data, which are not reported in official studies shall be revealed.

To obtain an objective impression of the current status of the community, several hundred posts from 93 topics on DEM generation with Sentinel-1 data were identified via the forum's search function and categorized regarding the content of the discussions and the main reasons why the approaches failed or did not produce the desired results. They are summarized in Figure 12,

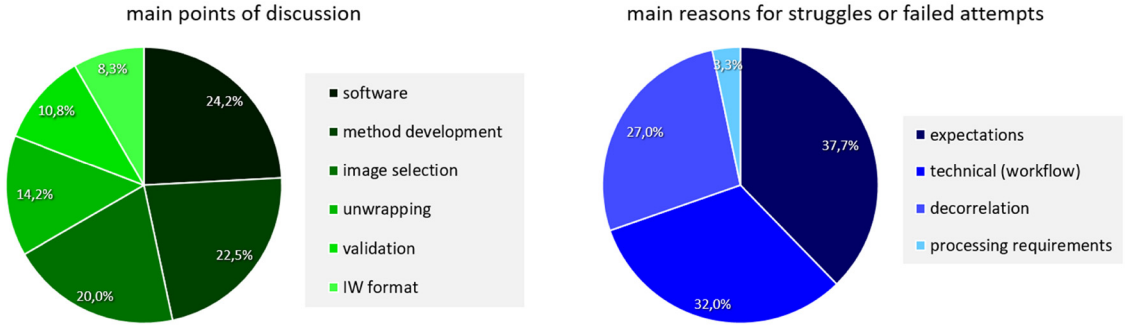

Figure 12: Results of the systematic evaluation of posts and topics related to DEM generation with Sentinel-1 data in the SNAP user forum.

as percentages because some of the forum posts could be of several categories and also include both content discussions (left) and error analysis (right). Unsurprisingly, the most frequent topic is the handling of the software itself (24.2%), dealing with the tools outlined in Figure 10, their order within the workflow, their implications, and the underlying parameters. The second most frequent topic was summarized under "method development," such as any approach going beyond this standard procedure, for example, by averaging DEMs of different interferograms, masking out low coherence areas or combining ascending and descending data (22.5%). The third point of equal importance was the selection of suitable images as input for the DEM generation (20.0%), indicating that the roles of perpendicular and temporal baselines are increasingly being considered in the study design. Other frequent topics dealt with the unwrapping process conducted outside the SNAP software based on the snaphu tool (see Figure 10), which brings its challenges (14.2%), ways of validating the generated result based on reference DEMs or field measurements (10.8%), and the specifications of the Sentinel-1 IW SLC products that consists of three sub-swaths and nine bursts, which have to be handled during the processing as outlined in Section 2.2. Accordingly, the forum serves as a platform for both the information on the correct processing steps and parameter settings and also for the exchange of ideas, strategies, and new methods, which emerge from the basic principles. Moreover, a closer look at these discussions also reveals the need for a concise description of the workflow tailored to Sentinel-1 data and the role of all involved parameters as presented in Section 2.1. Also note that, the users who are actively seeking help in the forum often lack clear guidance, for example, by lecturers or advisors or the exchange of expertise with colleagues.

Looking at the reasons why users struggle with DEM generation based on Sentinel-1 data or why they are not satisfied with the results, exaggerated expectations are the most frequent cause for their dissatisfaction (37.7%). This might be caused by the fact that SRTM is known to be derived from the radar data, and the free availability of Sentinel-1 data raises hopes to achieve something similar at higher quality. Although the spatial resolution of Sentinel-1 SLC data is 5 by 20 m in theory, the level of detail of the produced DEM is mostly lower than the one of freely available datasets, such as SRTM, ASTER GDEM, or AW3D30 (all around 30 m). The main reasons for this are phase decorrelation in vegetated areas, low fringe densities due to small height ambiguities (see Figure 7), or geometric effects (layover and shadow) in areas of extreme topography (see Figure 8). As many of the use cases are conducted within scientific theses, these overly high expectations were observed to be triggered by supervisors with no radar background who urged their students to produce higher quality DEMs compared to those globally available. In the end, only a few cases discussed in this forum could be considered successful in revealing land forms and height measurements, which can be used for subsequent tasks. The second leading reason for users struggling with this task is a lack of technical knowledge on the workflow and its components (32.0%). This again underlines the need for a clear and critical documentation of the processing as provided in this study. A third point, closely related to exaggerated expectations, is the role of the temporal phase decorrelation, leading to noisy interferograms without reliable information. However, it was frequently observed that the processing is continued even when the interferogram was obviously not suitable for height extraction, leading to artifacts during the filtering and randomly generated ramps after the unwrapping process. Again, a clear visual inspection and evaluation of the intermediate products checking for their correctness and integrity, such as demonstrated in Figure 4, has not always been conducted. Only a very small fraction of cases reported limitations (RAM or CPU) related to computationally intensive processing (3.3%).

These points confirm that the technical requirements of DEM generation with Sentinel-1 data with openly available software are widely given, but problems mostly occur based on little technical understanding or missing awareness of error sources.

4 Discussion

This section summarizes the most important points presented in this study and discuss them with respect to ongoing research and against current developments.

4.1 Minimum requirements and practice recommendations

It was confirmed in the example from Section 2.1 and the case studies evaluated in Section 3.2 that there are two points largely affecting the quality of the desired outcome: the first is temporal decorrelation, caused by the changing scattering mechanisms of surfaces between the first and the second image acquisition. The observed

phase decorrelation leads to noise in the interferogram, which then produces irregular height values after the unwrapping process. Although different computational solutions based on the statistical improvement of the phase image [167] or multitemporal approaches [168] have been proposed to overcome low coherence areas, the most effective method is to keep the temporal baseline as short as possible. With Sentinel-1A and 1B in orbit, the shortest repeat cycle of a track is 6 days for large parts of Europe and 12 days for the rest of the world [124]. Yet, as shown in many studies and demonstrated in Figure 5, temporal decorrelation of C-band radar data remains a problem, especially in areas with dense vegetation, where the factor of volume decorrelation additionally increases this phenomenon [169]. Currently, no solutions are provided to tackle this issue for image pairs separated by 6 or even 12 days. At least the effect of lower vegetation can be reduced by selecting images from the dry period, especially in the study areas with pronounced seasonality [170].

One way to address smaller segments of low coherence, such as that caused by water bodies, is to mask them before the unwrapping step, so that smaller areas of phase decorrelation can be compensated and will only lead to locally false height estimates. But these areas should neither dominate the image nor separate segments with good coherence because the subsequent cost-based unwrapping process will no longer be able to bypass these noisy parts, and will generate faulty results or arbitrary trends [127,171]. As shown in the literature review, if a certain density of vegetation is exceeded, results will become unusable regardless of the temporal baseline [145,148,151]. Accordingly, studies on forest areas based on repeat-pass Sentinel-1 imagery are not feasible with classic InSAR approaches. This is also supported by the evaluation of failed attempts reported in the SNAP user forum (Figure 12).

The second most important factor is the height ambiguity, which expresses the amount of topographic change represented by one fringe in the interferogram. It can be controlled by the selection of image pairs with large perpendicular baselines. As shown in Figure 7, a higher density of phase cycles allows a more precise description of height variations, which is achieved by selecting image pairs separated by at least 100 m or even better 150 m. As outlined in Section 2.1.4, these image pairs are not always easy to find because the orbital tube of Sentinel-1 was mainly designed to facilitate DInSAR approaches of displacement mapping where short perpendicular baselines are more favorable [84].

To assist the selection of suitable image pairs, the Alaska Satellite Facility provides a useful online tool, which enables the filtering of Sentinel-1 products [172], so that image pairs that fulfill the basic requirements for DEM generation can be identified. The plot on the bottom right of Figure 13 shows all available Sentinel-1 products belonging to the selected track (here: path 123) with the red point at 0 days and 0 m as the reference product, as it was used in this study (Table 1). All potential secondary images are located based on their temporal (*x*-axis) and

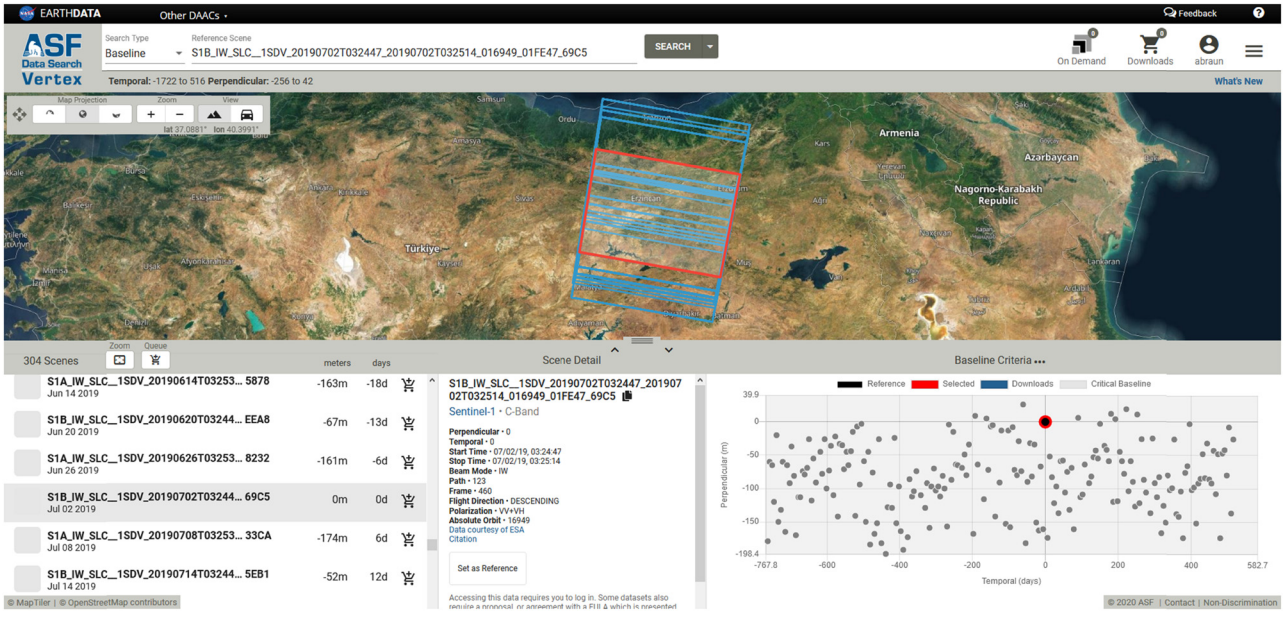

Figure 13: ASF baseline tool. Image used with courtesy of the Alaska Satellite Facility.

perpendicular baselines (y-axis). The exact values are given at the bottom right of the figure.

To minimize the effect of atmospheric disturbances of the phase signal, it is furthermore advisable to carefully check the weather conditions of the image acquisition days, especially as rain, snow, and wind cause a loss of coherence. Accordingly, images from the dry season should be preferred [59]. It was also found that the increased water vapor content on very hot days degrades the quality of the phase, so images acquired during night time could also be an alternative [173]. As stated in Section 2.1.5, the impact of atmospheric disturbances in single-pair interferograms is hard to estimate because unlike in DInSAR approaches, they are superimposed by the topographic phase component and cannot be estimated based on systematic time-series analyses of phase anomalies [113]. Yet, according to Zebker et al., their impact can reach up to 100 m of height difference [116]. A straightforward way of removing atmospheric disturbance for DEM generation is the simulation of φ_{atm}, with the Generic Atmospheric Correction Online Service for InSAR (GACOS [174]), which allows the estimation of the spatial pattern of tropospheric impact based on the weather forecast data, DEMs, and tropospheric delay as measured by a global network of GPS stations. It produces maps of zenith total tropospheric delay for any selectable date and acquisition time, which can be added to or subtracted from any calculated interferogram. However, its compatibility with interferograms calculated in SNAP has not been demonstrated yet.

Finally, users who are interested in special parts of the study area (e.g., glacier tongues, landslide areas, or moving dunes) should carefully select the flight direction of the satellite with respect to the right-looking acquisition geometry of Sentinel-1 satellites, because either the ascending or the descending track might be more favorable for the mapping of an area of interest in mountainous terrain. The effect of flight direction on the degree and spatial distribution of usable information for DEM generation has been systematically investigated by Eineder who proposes a solution to overcome errors in shadow areas for the later phase unwrapping step and names incidence angles near 45° as ideal for DEM generation [175]. Also, methods to combine ascending and descending passes have been proposed [71,110,176], but not yet demonstrated with Sentinel-1 data. To illustrate the impact of look direction on the interferometric quality of an acquisition, two coherence maps generated from image pairs of ascending and descending orbits are compared as presented in Table 1 (A1 and C1) and as a color composite in Figure 14. Both have a temporal baseline of 6 days to grant equal conditions regarding temporal decorrelation. This figure shows that coherence is equally high (white) and low (black) on flat terrain, but significantly differs for slopes facing toward the northwest and southeast. It was already demonstrated in Section 2.1.4 that slopes facing southeast lead to noise in the hillshade representation (Figure 7, descending data, A1). Accordingly, these slopes are yellow in Figure 14, indicating a largely higher coherence in the ascending data (C1).

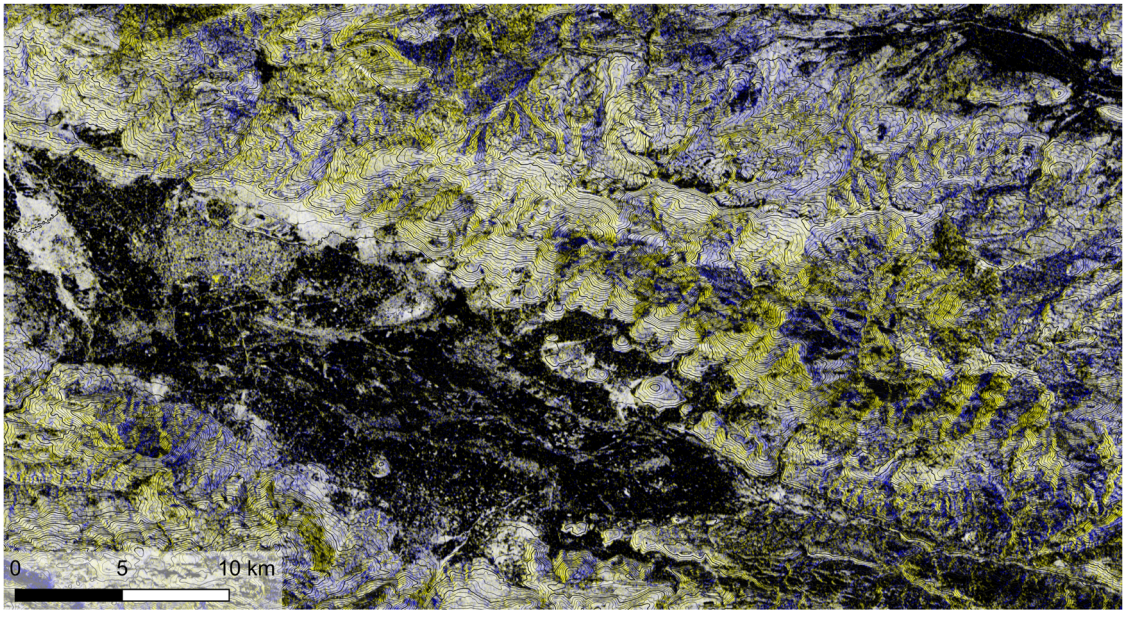

Figure 14: Coherence of an ascending (yellow) and descending (blue) image pair of the study area (both scaled between 0 and 1).

Generally, very large and very small local incidence angles lead to the largest RMSE estimates (Figure 8), so that a suitable satellite orbit (determining both incidence angle and look direction) should be carefully decided in advance.

Concludingly, with higher awareness of the presented requirements and limitations, the quality of interferometric DEMs retrieved from Sentinel-1 can be increased, and false expectations as reported in Figure 12 can be avoided.

4.2 Suggestions on good scientific practice

The evaluation of existing studies has shown that there is currently no agreed-upon code of conduct, which frames how InSAR-based height derivation is reported in a transparent and scientific way. This section, therefore, suggests a number of standards, which should be included to make the presented work repeatable and understandable in terms of quality assurance. This list is not meant to be exhaustive for this field of study, but rather intends to place a foundation for new discourse and extension.

1. Product IDs: The easiest and most transparent way to document input data is to list the product IDs as given in the metadata under *Abstracted metadata\PRODUCT*. This entry is unique and contains information on the mission, acquisition mode, acquisition date, and time, plus several other notations that help to characterize the data [177]. Furthermore, it facilitates quick access to the data in the official data hub [120] for an identical reproduction of the study, and the checking of the properties of image pairs in the ASF baseline tool [172].
2. Image dates and perpendicular baselines: As the first point seems obvious, it was shown in the literature survey that not all studies have provided information on the acquisition dates, which do not only have an impact on the temporal baseline but also if the pairs were selected based on climatic conditions as suggested in Section 4.1. Furthermore, the aspect of the perpendicular baseline was ignored or not reported to the readers in half of the examined studies (Figure 11). As these factors were found to be most limiting for the quality, which can be expected from such analyses, they should be clearly communicated in all scientific studies.
3. Preprocessing steps: Regardless of the software used, the TOPS format of Sentinel-1 requires some necessary steps as outlined in Figure 10. Accordingly, the selection of polarization, sub-swaths, and bursts should be given in any study, as well as the coregistration parameters of both the back geocoding (reference DEM) and ESD (registration width and cross-correlation threshold) operators. As multi-looking and filtering are optional, their usage for image enhancement should be documented as well as the parameters used during the unwrapping process, especially the initialization of the network by either a minimum spanning tree algorithm or a minimum cost flow algorithm [127]. An example for a clear declaration of all these steps is given by Sefercik et al. [141] who demonstrate how this helps to make the data preparation transparent and repeatable.
4. Interferogram and coherence: If a study deals with the derivation of height features from interferometric pairs, it is advisable to show the resulting interferogram in the area of interest, as well as the coherence layer. This not only helps to clarify the information content of the data but also highlights areas of potential errors. As these can propagate in the subsequent unwrapping step, it is also suggested to show the unwrapped phase before its translation to metric heights. As the visual inspection of the phase quality is a crucial part of interferometric processing, it is not advised to fully automate these tasks, because this prevents the identification of error sources [24,44,178].
5. Reference DEM: First, during the processing, a reference DEM is required for both back geocoding and range Doppler terrain correction. While the first step enables the precise coregistration of the reference and the secondary product, the latter is responsible for the precise geolocation of the derived DEM. Accordingly, the quality of the reference DEM has a strong impact on the InSAR results as well, and artifacts in the reference DEM can potentially introduce additional errors. Openly accessible DEMs, such as SRTM or AW3D30 at 30 m spatial resolution, are largely free of errors, but their quality should be checked for the respective study area, for example, by a systematic comparison and check [179]. Second, whenever a reference DEM is used to assess the accuracy of a generated InSAR DEM, it has to be made sure that the quality of the validation data is at least three times greater than the elevations being evaluated [4,178]. Only then it is granted that the accuracy measures are reliable. For DEMs derived from Sentinel-1, this would require a reference DEM with a spatial resolution of 3 m, which at least partially covers the produced result.
6. Accuracy assessment: Most of the evaluated studies have performed a statistical or visual validation. However, many of them also agree that only a

combination of measures will really reveal if the generated DEM is precise and useful. MAE and RMSE are the most used approaches because their computations are based on a reference DEM or GPS points, which are straightforward and give a measure of deviation in meters, which is easy to interpret. However, they do not reveal the presence of systematic errors, spatial patterns, or atmospheric artifacts in the data. Therefore, it is advisable to also provide maps of the result to visualize the final product, especially hillshade representations that can highlight noisy areas and regular patterns much better than color-coded elevations [180] and best when compared with those of a reference DEM of higher quality [1]. In addition, Podobnikar presents a number of approaches for the visual check for errors in interferograms [181].

7. Purpose: Finally, the success of a proposed approach to generate a DEM from Sentinel-1 data should always be measured by the question of it is both correct and useful. While the first measure refers to the statistical accuracy, the second is of a rather qualitative nature and linked to the purpose of DEM generation. A dataset is only considered useful if it delivers the information required for a specific task [182]. For example, an R^2 of 0.98 assessed by 1,000 reference points collected over the entire image is meaningless if the purpose is to estimate tree heights where the investigated forest areas suffer from phase decorrelation. Furthermore, it should be always evaluated if the generated DEM outperforms the currently available datasets for the desired purpose (e.g., spatial resolution, temporal validity, or higher vertical accuracy). Accordingly, the authors are encouraged to discuss their results based on both quantitative and qualitative criteria.

4.3 Open points and outlook

This study showed that it is possible to generate DEMs based on Sentinel-1 radar interferometry, given that basic requirements are met, most importantly the length of temporal and perpendicular baselines. While the first baseline controls the expected amount of temporal decorrelation over natural surfaces, the second determines the amount of height, which is represented by the one-phase cycle. If these things are considered in advance as outlined in Section 2.1 and implemented as suggested in Section 4.1, the technical conditions are fulfilled to generate DEMs at a spatial resolution of nearly 10 m, which exceed the detail provided by openly available DEMs, such as SRTM, ASTER, and AW3D30. However, from the perspective of the study site, this approach is condemned to fail in areas with large and dense vegetation cover, because the current repeat cycle of 6 days and the wavelength of around 5 cm are too sensitive to the altering scattering mechanisms of shrubs, cropland, forest canopies, and wetlands. Systematic investigations on the loss of coherence are shown in Figure 5, and more extensive studies are presented by Jacob et al. and Mestre-Quereda et al. [78,183]. As suggested in Section 4.2, the authors of future studies on this topic are encouraged to discuss the impact of different parameters in general, and specifically, for their study area and target information (topographic height vs surface height), as this has been found to be a clear shortcoming in the presented literature review.

The most striking open points with respect to data processing identified in this study are briefly as follows: First, ways to reduce atmospheric impacts are only provided in DInSAR studies where the effect of topography is excluded [174,184], not for the purpose of DEM generation. Workflows to directly integrate tropospheric delay maps from GACOS [174] or TRAIN [185] would certainly increase the accuracy in latitudes with generally high water vapor contents.

Second, only few studies investigated the impact of horizontal inaccuracies occurring in different steps over the workflow. Ahmadabadi et al. underlined the necessity to coregister radar images with optical sensors for the best exploitation of information [159]. Also Dabiri et al. performed a spatial adjustment of the pre- and post-landslide DEM to avoid misinterpretations of false volume changes caused by horizontal shifts [156]. Atalay and Sefercik performed registration of the generated DEM with the reference DEM to reduce the impact of geometric effects caused by the side-looking SAR geometry [140]. Accordingly, any study that creates DEMs of several dates or merges them with other data in subsequent analysis steps, should make sure that errors resulting from misregistration are minimized [186].

Thirdly, instead of single-pair approaches, methods to merge images of multiple dates, incidence angles, and look directions, should be brought into focus by the future study. Methods of merging image parts with high accuracies can be based on coherence estimates [94] or height accuracy maps, as already proposed for Sentinel-1 data by Nikolakopoulos and Kyriou [152,157,158]. Again, openly accessible and standardized workflows are to be developed to fully exploit the current database with hundreds of Sentinel-1 products of most parts of the Earth (Figure 9).

One point that makes the comparison of the presented studies difficult is the variety of accuracy measures (Table 4). One reason for this is the heterogeneity of reference data, which come at different spatial resolutions (in terms of DEMs) and in different numbers (GCPs collected in the field). As these reference data mostly follow unequal distributions, Willmott and Matsuura argue that the RMSE is not suitable for many environmental studies [187]. They suggest the MAE as a more natural measure, which is unambiguous and less sensitive to the distributions of the error magnitudes.

As mentioned in many studies and supported in Section 4.2, single accuracy measures are often not sufficient to reveal if the data are both accurate and free of errors. For this reason, Höhle and Höhle suggest checking for various types of errors [178]: RMSE, non-normal error distributions (skewness, kurtosis, and outliers by histogram comparisons, quantiles median, and NMAD), and statistical tests for significance (null hypothesis: no difference between the reference and InSAR DEM). To add to this, the impact of the sample size and distribution is discussed as initially proposed by Story and Congalton in 1986 and 2001 [188,189]. Besides these aspects, Liu and Jezek propose a way to assess the anisotropy of errors in DEMs based on directional variograms and Fourier analysis [190] as a more systematic approach to assess shortcomings caused by the side-looking geometry of the SAR system. An even more comprehensive list and comparison of uncertainty measures for DEM data and the role of statistical significance are presented by Wechsler, and Wechsler and Kroll [191,192]. It is the responsibility of the authors to identify those which are the most meaningful, robust, and honest for the respective study.

Future research could investigate, which approaches of interferogram stacking, as suggested by Ferretti et al. [59], are the most applicable for Sentinel-1 TOPS data. This addresses the question concerning which forms of merging (masking, averaging, or weighting) lead to the best quality with respect to low coherence areas, but also whether single or multi-baseline approaches are the most promising [114]. Undoubtedly, the full potential of the magnitude of openly accessible Sentinel-1 products is currently not completely exploited. First steps in this direction were proposed by Crosetto et al. who indicate the tomographic capabilities of Sentinel-1 data for urban height detection based on 61 image products [193]. Currently, the orbital tube of Sentinel-1 is too narrow for effective application of SAR tomography, but first approaches have been developed [194] in case this will change for future missions. Hence, it was proposed by Giudici et al. to reduce the repeat cycle of the mission with the upcoming Sentinel-1C and D or even design it as a tandem mission with a larger perpendicular baseline [195].

With Sentinel-1, we have entered the *Big InSAR Data Era*, as postulated by Minh et al., which brings a new quality to the analyses with respect to data availability, acquisition, and continuity [196]. The intention of this study was to clarify its capabilities regarding DEM generation, which are limited by certain parameters, thus relying on creativity and awareness of error sources if new and successful approaches will be developed in the future.

Acknowledgments: Sentinel-1 data were provided by the European Space Agency (ESA) within the Copernicus Programme. The author also thanks the developers of the Sentinel Application Toolbox (SNAP) for their tremendous contribution to the field of open geospatial scientific analyses. Further thanks go to Edward Cahill for the language editing of the article. We acknowledge support by the Open Access Publishing Fund of the University of Tübingen. The author has signed the joint statement of WInSAR, COMET, and MDIS released in summer 2020 supporting the replacement of the previously used master/slave terminology to promote equality and inclusion in the scientific community. https://comet.nerc.ac.uk/about-comet/insar-terminology/

Funding information: This study received no external funding.

Author contribution: All contents were developed, researched, and written by Andreas Braun.

Conflict of interest: The author states no conflict of interest.

References

[1] Schillaci C, Braun A, Kropáček J. Terrain analysis and landform recognition. In: Cook SJ, Clarke LE, Nield J, editors. Geomorphological techniques: online edition. London: British Society for Geomorphology; 2012. p. 1–18.

[2] Martz LW, Garbrecht J. Numerical definition of drainage network and subcatchment areas from digital elevation models. Comput Geosci. 1992;18:747–61.

[3] Lee J. Digital analysis of viewshed inclusion and topographic features on digital elevation models. Photogram Eng Remote Sens. 1994;60:451–556.

[4] Maune DF. Digital elevation model technologies and applications: the DEM users manual. 2nd edn. Bethesda: ASPRS; 2007.
[5] Moore ID, Grayson RB, Ladson AR. Digital terrain modelling: a review of hydrological, geomorphological, and biological applications. Hydrolog Process. 1991;5:3–30.
[6] Finsterwalder R, Frieser H, Schmidt-Kraepelin E. Photogrammetrie. 3rd edn. Berlin: De Gruyter; 1968.
[7] Miller CL, Laflamme RA. The digital terrain model: theory and application. Photogram Eng. 1958;24:433–42.
[8] Doyle FJ. Digital terrain models: an overview. Photogram Eng Remote Sens. 1978;44:1481–5.
[9] Linder W. Digital photogrammetry: a practical course. Berlin, Heidelberg: Springer-Verlag Berlin Heidelberg; 2006.
[10] Deilami K, Hashim M. Very high resolution optical satellites for DEM generation: a review. Eur J Sci Res. 2011;49:542–54.
[11] Helpke C. State-of-the-art of digital photogrammetric workstations for topographic applications. Photogram Eng Remote Sens. 1995;61:49–56.
[12] Hannah MJ. Digital stereo image matching techniques. Int Arch Photogram Remote Sens. 1988;27:280–93.
[13] ASTER NASA. Global Digital Elevation Model (GDEM); 2019. https://lpdaac.usgs.gov/products/astgtmv003/ Accessed 15 May 2020.
[14] Tadono T, Ishida H, Oda F, Naito S, Minakawa K, Iwamoto H. Precise global DEM generation by ALOS PRISM. ISPRS annals of the photogrammetry. Remote Sens Spat Inf Sci. 2014;2:71.
[15] NASA. EarthData portal; 2020. https://search.earthdata.nasa.gov. Accessed 15 May 2020.
[16] JAXA. ALOS Global Digital Surface Model "ALOS World 3D – 30m (AW3D30)"; 2020. https://www.eorc.jaxa.jp/ALOS/en/aw3d30/. Accessed 15 May 2020.
[17] Kraus K, Pfeifer N. Advanced DTM generation from LIDAR data. International archives of the photogrammetry, remote sensing and spatial. Inf Sci. 2001;34:23–30.
[18] Demir N, Poli D, Baltsavias E. Extraction of buildings and trees using images and LiDAR data. International archives of the photogrammetry. Remote Sens Spat Inf Sci. 2008;37:313–8. doi: 10.3929/ethz-b-000011960.
[19] Graham LC. Synthetic interferometer radar for topographic mapping. Proc IEEE. 1974;62:763–8.
[20] Prati C, Rocca F. Limits to the resolution of elevation maps from stereo SAR images. Int J Remote Sens. 1990;11:2215–35. doi: 10.1080/01431169008955171.
[21] Ostrowski JA, Cheng P. DEM extraction from stereo SAR satellite imagery. IEEE International Geoscience and Remote Sensing Symposium; 24–28 July 2000. Honolulu: IEEE; 2000. p. 2176–8. doi: 10.1109/IGARSS.2000.858347.
[22] Kervyn F. Modelling topography with SAR interferometry: illustrations of a favourable and less favourable environment. Comput Geosci. 2001;27:1039–50.
[23] Madsen SN, Zebker HA, Martin J, Madsen SN, Zebker HA, Martin J. Topographic mapping using radar interferometry: processing techniques. IEEE Trans Geosci Remote Sens. 1993;31:246–56. doi: 10.1109/36.210464.
[24] Hanssen RF. Radar interferometry: data interpretation and error analysis. Dordrecht, Netherlands: Kluwer Academic Publishers; 2001. 328 pp.
[25] Bamler R, Hartl P. Synthetic aperture radar interferometry. Inverse Probl. 1998;14:R1–54.
[26] Small D. Generation of digital elevation models through spaceborne SAR interferometry. Doctoral dissertation/PhD. Zürich: University of Zürich; 1998.
[27] Massonnet D, Rabaute T. Radar interferometry: limits and potential. IEEE Trans Geosci Remote Sens. 1993;31:455–64.
[28] Rabus B, Eineder M, Roth A, Bamler R. The shuttle radar topography mission. A new class of digital elevation models acquired by spaceborne radar. ISPRS J Photogram Remote Sens. 2003;57:241–62. doi: 10.1016/S0924-2716(02)00124-7.
[29] NASA JPL. NASA Shuttle Radar Topography Mission Global 1 arc second; 2013. Accessed 15 May 2020.
[30] Yang L, Meng X, Zhang X. SRTM DEM and its application advances. Int J Remote Sens. 2011;32:3875–96.
[31] Zandbergen P. Applications of shuttle radar topography mission elevation data. Geogr Compass. 2008;2:1404–31.
[32] Zink M, Bachmann M, Brautigam B, Fritz T, Hajnsek I, Moreira A, et al. TanDEM-X: the new global DEM takes shape. IEEE Geosci Remote Sens Mag. 2014;2:8–23.
[33] Huber M, Gruber A, Wendleder A, Wessel B, Roth A, Schmitt A. The global TanDEM-X DEM: production status and first validation results. International archives of the photogrammetry, remote sensing and spatial information science; 25 August–01 September 2012, Melbourne: International Society for Photogrammetry and Remote Sensing (ISPRS); 2012. p. 45–50.
[34] DLR. The TanDEM-X 90m digital elevation model; 2020. https://geoservice.dlr.de/web/dataguide/tdm90/. Accessed 15 May 2020.
[35] Rodriguez E, Morris CS, Belz JE. A global assessment of the SRTM performance. Photogram Eng Remote Sens. 2006;72:249–60.
[36] Wessel B, Huber M, Wohlfart C, Marschalk U, Kosmann D, Roth A. Accuracy assessment of the global TanDEM-X digital elevation model with GPS data. ISPRS J Photogram Remote Sens. 2018;139:171–82. doi: 10.1016/j.isprsjprs.2018.02.017.
[37] van Zyl JJ. The Shuttle Radar Topography Mission (SRTM): a breakthrough in remote sensing of topography. Acta Astron. 2001;48:559–65.
[38] Potin P, Rosich B, Miranda N, Grimont P, Shurmer I, O'Connell A, et al. Copernicus Sentinel-1 constellation mission operations status. IEEE International Geoscience and Remote Sensing Symposium; 28 July–02 September 2019. Yokohama: IEEE; 28 July–02 September 2019. p. 5385–8. doi: 10.1109/IGARSS.2019.8898949.
[39] Geudtner D, Torres R, Snoeij P, Davidson M, Rommen B. Sentinel-1 system capabilities and applications. IEEE International Geoscience and Remote Sensing Symposium; 13–18 July 2014. Quebec City: IEEE; 2014. p. 1457–60. doi: 10.1109/IGARSS.2014.6946711.
[40] Kovács IP, Bugya T, Czigány S, Defilippi M, Lóczy D, Riccardi P, et al. How to avoid false interpretations of Sentinel-1A TOPSAR interferometric data in landslide mapping? Hungary: a case study: recent landslides in Transdanubia. Nat Hazards. 2019;96:693–712. doi: 10.1007/s11069-018-3564-9.

[41] Zebker HA, Goldstein RM. Topographic mapping from interferometric synthetic aperture radar observations. J Geophys Res: Solid Earth. 1986;91:4993–9.
[42] Gens R, van Genderen JL. SAR interferometry: Issues, techniques, applications. Int J Remote Sens. 1996;17:1803–35. doi: 10.1080/01431169608948741.
[43] Pinheiro M, Reigber A, Moreira A. Large-baseline InSAR for precise topographic mapping: a framework for TanDEM-X large-baseline data. Adv Radio Sci. 2017;15:231–41.
[44] Bürgmann R, Rosen PA, Fielding EJ. Synthetic aperture radar interferometry to measure Earth's surface topography and its deformation. Annu Rev Earth Planet Sci. 2000;28:169–209.
[45] Parizzi A, Perissin D, Prati C, Rocca F, Ferretti A. Accurate DEM Reconstruction from Permanent Scatterers and Multi-baseline Interferometry. IEEE International Geoscience and Remote Sensing Symposium; 31 July–04 August 2006. Denver: IEEE; 2006; p. 157–60. doi: 10.1109/IGARSS.2006.45.
[46] Zebker HA, Villasenor J. Decorrelation in interferometric radar echoes. IEEE Trans Geosci Remote Sens. 1992;30:950–9.
[47] Ferretti A, Monti-Guarnieri A, Prati C, Rocca F. InSAR processing: part C: a mathematical approach. Noordwijk, The Netherlands: ESA Publications; 2007.
[48] Ferretti A, Monti-Guarnieri A, Prati C, Rocca F, Massonnet D. InSAR principles: part A: guidelines for SAR interferometry processing and interpretation. Noordwijk, The Netherlands: ESA Publications; 2007.
[49] Li Z, Bethel J. Image coregistration in SAR interferometry. The International Archives of the Photogrammetry. Remote Sens Spat Inf Sci. 2008;37:433–8.
[50] Li D, Zhang Y. A fast offset estimation approach for InSAR image subpixel registration. IEEE Geosci Remote Sens Lett. 2011;9:267–71.
[51] Scheiber R, Moreira A. Coregistration of interferometric SAR images using spectral diversity. IEEE Trans Geosci Remote Sens. 2000;38:2179–91.
[52] Foster MR, Guinzy NJ. The coefficient of coherence; its estimation and use in geophysical data processing. Geophysics. 1967;32:602–16.
[53] Wang T, Liao M, Perissin D. InSAR Coherence-Decomposition Analysis. IEEE Geosci Remote Sens Lett. 2010;7:156–60. doi: 10.1109/LGRS.2009.2029126.
[54] Santoro M, Wegmüller U, Askne JIH. Signatures of ERS-Envisat interferometric SAR coherence and phase of short vegetation: an analysis in the case of maize fields. IEEE Trans Geosci Remote Sens. 2010;48:1702–13. doi: 10.1109/TGRS.2009.2034257.
[55] Dehecq A, Millan R, Berthier E, Gourmelen N, Trouvé E, Vionnet V. Elevation changes inferred from TanDEM-X data over the Mont-Blanc area: Impact of the X-band interferometric bias. IEEE J Sel Top Appl Earth Obser Remote Sens. 2016;9:3870–82.
[56] Crosetto M, Crippa B. Optical and radar data fusion for DEM generation. ISPRS Commission IV Symposium on GIS; 7–10 September 1998, Stuttgart: International Society for Photogrammetry and Remote Sensing (ISPRS); 1998. p. 128–34.
[57] Crosetto M. Calibration and validation of SAR interferometry for DEM generation. ISPRS J Photogram Remote Sens. 2002;57:213–27. doi: 10.1016/S0924-2716(02)00107-7.
[58] Zebker HA, Lu Y. Phase unwrapping algorithms for radar interferometry: residue-cut, least-squares, and synthesis algorithms. JOSA A. 1998;15:586–98.
[59] Ferretti A, Monti-Guarnieri A, Prati C, Rocca F. InSAR processing: part B: a practical approach. Noordwijk, The Netherlands: ESA Publications; 2007.
[60] Goldstein RM, Zebker HA, Werner CL. Satellite radar interferometry: two-dimensional phase unwrapping. Radio Sci. 1988;23:713–20. doi: 10.1029/RS023i004p00713.
[61] Goldstein RM, Werner CL. Radar interferogram filtering for geophysical applications. Geophys Res Lett. 1998;25:4035–8. doi: 10.1029/1998GL900033.
[62] Li ZW, Ding XL, Huang C, Zhu JJ, Chen YL. Improved filtering parameter determination for the Goldstein radar interferogram filter. ISPRS J Photogram Remote Sens. 2008;63:621–34.
[63] Zhu D, Zhu Z, Xie Q. A topography adaptive interferogram filter based on local frequency estimation. Acta Electron Sin. 2002;30:1853–6.
[64] Song R, Guo H, Liu G, Perski Z, Fan J. Improved Goldstein SAR interferogram filter based on empirical mode decomposition. IEEE Geosci Remote Sens Lett. 2013;11:399–403.
[65] Baran I, Stewart MP, Kampes BM, Perski Z, Lilly P. A modification to the Goldstein radar interferogram filter. IEEE Trans Geosci Remote Sens. 2003;41:2114–8.
[66] Richards MA. A beginner's guide to interferometric SAR concepts and signal processing. IEEE Aerosp Electron Syst Mag. 2007;22:5–29.
[67] Madsen SN, Zebker HA. Automated absolute phase retrieval in across-track interferometry. IEEE International Geoscience and Remote Sensing Symposium; 26–29 May 1992. Houston: IEEE; 1992; p. 1582–4.
[68] Schreier G. SAR geocoding: data and systems. Karlsruhe: Wichmann;; 1993.
[69] Liang C, Li Y, Luo J. Interferometric processing of Sentinel-1 TOPS data. IEEE Trans Geosci Remote Sens. 2016;54:2220–34. doi: 10.1109/TGRS.2015.2497902.
[70] Askne JIH, Dammert PBG, Ulander LMH, Smith G. C-band repeat-pass interferometric SAR observations of the forest. IEEE Trans Geosci Remote Sens. 1997;35:25–35.
[71] Sansosti E, Lanari R, Fornaro G, Franceschetti G, Tesauro M, Puglisi G, et al. Digital elevation model generation using ascending and descending ERS-1/ERS-2 tandem data. Int J Remote Sens. 1999;20:1527–47.
[72] Wegmüller U, Santoro M, Werner CL, Strozzi T, Wiesmann A, Lengert W. DEM generation using ERS-ENVISAT interferometry. J Appl Geophysics. 2009;69:51–8.
[73] Colesanti C, Zan FDe, Prati C, Rocca F. Generation of DEM with sub-metric vertical accuracy from 30'ERS-ENVISAT pairs. FRINGE workshop; 1–5 December 2003, Frascati: European Space Agency (ESA); 2003. p. 1–5.
[74] Hong S, Won J. ERS-ENVISAT cross-interferometry for coastal DEM construction. FRINGE workshop; 28 November–2 December 2005, Frascati: European Space Agency (ESA); 2005. p. 1–6.
[75] Goldstein RM. Atmospheric limitations to repeat-track radar interferometry. Geophys Res Lett. 1995;22:2517–20.
[76] Morishita Y, Hanssen RF. Temporal decorrelation in L-, C-, and X-band satellite radar interferometry for pasture on drained peat soils. IEEE Trans Geosci Remote Sens. 2014;53:1096–104.

[77] EEA. https://land.copernicus.eu/pan-european/corine-land-cover/clc2018
[78] Jacob AW, Vicente-Guijalba F, Lopez-Martinez C, Lopez-Sanchez JM, Litzinger M, Kristen H, et al. Sentinel-1 InSAR coherence for land cover mapping: a comparison of multiple feature-based classifiers. IEEE J Sel Top Appl Earth Observ Remote Sens. 2020;13:535–52.
[79] Vicente-Guijalba F, Jacob A, Lopez-Sanchez JM, Lopez-Martinez C, Duro J, Notarnicola C, et al. Sincohmap: land-cover and vegetation mapping using multi-temporal Sentinel-1 interferometric coherence. IEEE International Geoscience and Remote Sensing Symposium; 22–27 July 2018, Valencia, Spain: Institute of Electrical and Electronics Engineers (IEEE); 2018. p. 6631–4. doi: 10.1109/IGARSS.2018.8517926.
[80] ESA. Sentinels POD service file format specifications: revision 22 (18.01.2018), Frascati: European Space Agency (ESA); 2011.
[81] Schubert A, Small D, Meier E, Miranda N, Geudtner D. Spaceborne SAR product geolocation accuracy: a Sentinel-1 update. IEEE International Geoscience and Remote Sensing Symposium; 13–18 July 2014. Quebec City: Institute of Electrical and Electronics Engineers (IEEE); 2014. p. 2675–8.
[82] Prats-Iraola P, Nannini M, Yagüe-Martínez N, Pinheiro M, Kim J-S, Vecchioli F, et al. Interferometric investigations with the Sentinel-1 constellation. IEEE International Geoscience and Remote Sensing Symposium; 23–28 July 2017. Fort Worth: IEEE; 23–28 July 2017. p. 5537–40. doi: 10.1109/IGARSS.2017.8128258.
[83] Barat I, Prats-Iraola P, Duesmann B, Geudtner D. Sentinel-1: link between orbit control and interferometric SAR baselines performance. 25th International Symposium on Space Flight Dynamics; 19–23 October 2015, Munich: German Space Operations Center (GSOC); 2015. p. 1–11.
[84] Prats-Iraola P, Rodriguez-Cassola M, Zan F, de Scheiber R, López-Dekker P, Barat I, et al. Role of the orbital tube in interferometric spaceborne SAR missions. IEEE Geosci Remote Sens Lett. 2015;12:1486–90.
[85] Hajduch G, Vincent P, Meadows P, Small D, Pilgrim A, Schubert A, et al. Sentinel-1 annual performance report 2019: version 1.1. Ramonville-Saint-Agne, France: Collecte Localisation Satellites; 2020.
[86] Liao M, Wang T, Lu L, Zhou W, Li D. Reconstruction of DEMs from ERS-1/2 tandem data in mountainous area facilitated by SRTM data. IEEE Trans Geosci Remote Sens. 2007;45:2325–35. doi: 10.1109/TGRS.2007.896546.
[87] Rufino G, Moccia A, Esposito S. DEM generation by means of ERS tandem data. IEEE Trans Geosci Remote Sens. 1998;36:1905–12. doi: 10.1109/36.729362.
[88] Shiping S. DEM generation using ERS-1/2 interferometric SAR data. IEEE International Geoscience and Remote Sensing Symposium; 24–28 July 2000. Honolulu: IEEE; 2000. p. 788–90.
[89] Knöpfle W, Strunz G, Roth A. Mosaicking of digital elevation models derived by SAR interferometry. Int Arch Photogram Remote Sens. 1998;32:306–13.
[90] Arnaud A, Adam N, Hanssen RF, Inglada J, Duro J, Closa J, et al. ASAR ERS interferometric phase continuity. IEEE International Geoscience and Remote Sensing Symposium; 21–25 July 2003. Toulouse: IEEE; 2003. p. 1133–5. doi: 10.1109/IGARSS.2003.1294373.
[91] Wegmüller U, Santoro M, Werner CL, Strozzi T, Wiesmann A. Estimation of ice thickness of tundra lakes using ERS – ENVISAT cross-interferometry. IEEE International Geoscience and Remote Sensing Symposium; 25–30 July 2010. Honolulu: IEEE; 25–30 July 2010. p. 316–9. doi: 10.1109/IGARSS.2010.5649026.
[92] Wegmüller U, Santoro M. ERS-ENVISAT Cross-Interferometry results over Egypt Proc Fringe 2010. FRINGE workshop; 30 November–4 December 2009, Frascati: European Space Agency (ESA); 2009. p. 1–5.
[93] Gasparetto-Stori G, Strozzi T, Teatini P, Tosi L, Vianello A, Wegmüller U. DEM of the Veneto plain by ERS2-ENVISAT cross-interferometry. 7th EUropean congress on REgional GEOscientific cartography and Information systems; 12–15 June 2012, Bologna: Bayerisches Landesamt für Umwelt; 2012. p. 349–50.
[94] Gelautz M, Paillou P, Chen CW, Zebker HA. Radar stereo- and interferometry-derived digital elevation models: comparison and combination using Radarsat and ERS-2 imagery. Int J Remote Sens. 2003;24:5243–64. doi: 10.1080/0143116031000115139.
[95] Geudtner D, Vaehon PW, Mattar KE, Gray AL. RADARSAT repeat-pass SAR interferometry. IEEE International Geoscience and Remote Sensing Symposium; 10 July 1998. Vol. 3. Seattle: IEEE; 10 July 1998. p. 1635–7. doi: 10.1109/IGARSS.1998.691661.
[96] Bueso-Bello J-L, Martone M, Prats-Iraola P, Bräutigam B. First characterization and performance evaluation of bistatic TanDEM-X experimental products. IEEE J Sel Top Appl Earth Observ Remote Sens. 2015;9:1058–71.
[97] Bamler R, Adam N, Davidson GW, Just D. Noise-induced slope distortion in 2-D phase unwrapping by linear estimators with application to SAR interferometry. IEEE Trans Geosci Remote Sens. 1998;36:913–21. doi: 10.1109/36.673682.
[98] Singh LP, van Westen CJ, Ray PC, Pasquali P. Accuracy assessment of InSAR derived input maps for landslide susceptibility analysis: a case study from the Swiss Alps. Landslides. 2005;2:221–8.
[99] Shirzaei M, Walter TR. Estimating the effect of satellite orbital error using wavelet-based robust regression applied to InSAR deformation data. IEEE Trans Geosci Remote Sens. 2011;49:4600–5.
[100] Yagüe-Martínez N, Zan FDe, Prats-Iraola P. Coregistration of interferometric stacks of Sentinel-1 TOPS data. IEEE Geosci Remote Sens Lett. 2017;14:1002–6.
[101] Prats-Iraola P, Nannini M, Scheiber R, Zan FDe, Wollstadt S, Minati F, et al. Sentinel-1 assessment of the interferometric wide-swath mode. IEEE International Geoscience and Remote Sensing Symposium; 26–31 July 2015. Milan, Italy: IEEE; 2015. p. 5247–51. doi: 10.1109/IGARSS.2015.7327018.
[102] Grandin R. Interferometric processing of SLC Sentinel-1 TOPS data. FRINGE 2015; 23–27 March 2015. Frascati, Italy: European Space Agency; 2015. doi: 10.5270/Fringe2015.pp116.
[103] Zhang W, Wang W, Chen L. Constructing DEM based on InSAR and the relationship between InSAR DEM's precision and terrain factors. Energy Proc. 2012;16:184–9.

[104] Bayer T, Schreier G, Winter R. Terrain influences in SAR backscatter and attempts to their correction. IEEE Trans Geosci Remote Sens. 1991;29:451–62.
[105] Eineder M, Holzner J. Interferometric DEMs in Alpine terrain: limits and options for ERS and SRTM. IEEE International Geoscience and Remote Sensing Symposium; 24–28 July 2000. Honolulu: IEEE; 2000; p. 3210–2.
[106] Breidenbach J, Koch B, Kändler G, Kleusberg A. Quantifying the influence of slope, aspect, crown shape and stem density on the estimation of tree height at plot level using lidar and InSAR data. Int J Remote Sens. 2008;29:1511–36.
[107] Derauw D. Phasimétrie par Radar à Synthèse d'Ouverture; théorie et applications. Doctoral dissertation/PhD. Liege: Faculté de Sciences; 1999.
[108] Eineder M, Suchandt S. Recovering radar shadow to improve interferometric phase unwrapping and dem reconstruction. IEEE Trans Geosci Remote Sens. 2003;41:2959–62. doi: 10.1109/TGRS.2003.821266.
[109] Gruber A, Wessel B, Martone M, Roth A. The TanDEM-X DEM mosaicking: fusion of multiple acquisitions using InSAR quality parameters. IEEE J Sel Top Appl Earth Observations Remote Sens. 2015;9:1047–57.
[110] Eineder M, Adam N, Naito S. Avoiding phase unwrapping in DEM generation by fusing multi frequency ascending and descending interferograms. IEEE International Geoscience and Remote Sensing Symposium; 20–24 September 2004. Anchorage: IEEE; 20–24 September 2004. p. 477–80. doi: 10.1109/IGARSS.2004.1369067.
[111] Zebker HA, Werner CL, Rosen PA, Hensley S. Accuracy of topographic maps derived from ERS-1 interferometric radar. IEEE Trans Geosci Remote Sens. 1994;32:823–36. doi: 10.1109/36.298010.
[112] Lazecký M, Hlaváčová I, Martinovič J, Ruiz-Armenteros AM. Accuracy of Sentinel-1 interferometry monitoring system based on topography-free phase images. Proc Comput Sci. 2018;138:310–7. doi: 10.1016/j.procs.2018.10.044.
[113] Ding X, Li Z, Zhu J, Feng G, Long J. Atmospheric effects on InSAR measurements and their mitigation. Sensors. 2008;8:5426–48.
[114] Ferretti A, Prati C, Rocca F. Multibaseline InSAR DEM reconstruction: the wavelet approach. IEEE Trans Geosci Remote Sens. 1999;37:705–15.
[115] Foster J, Brooks B, Cherubini T, Shacat C, Businger S, Werner CL. Mitigating atmospheric noise for InSAR using a high resolution weather model. Geophys Res Lett. 2006;33:L16304.
[116] Zebker HA, Rosen PA, Hensley S. Atmospheric effects in interferometric synthetic aperture radar surface deformation and topographic maps. J Geophys Res: Solid Earth. 1997;102:7547–63.
[117] Liang C, Agram P, Simons M, Fielding EJ. Ionospheric correction of InSAR time series analysis of C-band Sentinel-1 TOPS data. IEEE Trans Geosci Remote Sens. 2019;57:6755–73. doi: 10.1109/TGRS.2019.2908494.
[118] Brcic R, Parizzi A, Eineder M, Bamler R, Meyer F. Ionospheric effects in SAR interferometry: an analysis and comparison of methods for their estimation. IEEE International Geoscience and Remote Sensing Symposium; 24–29 July 2011. Vancouver, Canada: IEEE; 2011. p. 1497–500.
[119] Gomba G, Rodriguez Gonzalez F, Zan FDe. Ionospheric phase screen compensation for the Sentinel-1 TOPS and ALOS-2 ScanSAR modes. IEEE Trans Geosci Remote Sens. 2017;55:223–35. doi: 10.1109/TGRS.2016.2604461.
[120] ESA. Copernicus Open Access Hub; 2020. https://scihub.copernicus.eu/. Accessed 150.5.2020.
[121] ESA. ESA Online Dissemination; 2020. https://esar-ds.eo.esa.int/oads/access/. Accessed 15 May 2020.
[122] Aschbacher J. ESA's earth observation strategy and Copernicus. In: Onoda M, Young OR, editors. Satellite earth observations and their impact on society and policy. Singapore: Springer; 2017. p. 81–5.
[123] Knowelden R, Castriotta AG. Copernicus Sentinel data access; 2020. https://scihub.copernicus.eu/reportsandstats/. Accessed 15 Jun 2020.
[124] ESA. Sentinel High Level Operations Plan (HLOP); 2020. https://sentinel.esa.int/web/sentinel/missions/sentinel-1/observation-scenario. Accessed 15 May 2020.
[125] ESA. S1TBX – ESA Sentinel-1 Toolbox; 2020. http://step.esa.int. Accessed 15 May 2020.
[126] ESA. Over 500K downloads for ESA's SNAP toolbox;. 2020. http://www.esa.int/Applications/Observing_the_Earth/Over_500K_downloads_for_ESA_s_SNAP_toolbox. Accessed 15 May 2020.
[127] Chen CW, Zebker HA. Phase unwrapping for large SAR interferograms: statistical segmentation and generalized network models. IEEE Trans Geosci Remote Sens. 2002;40:1709–19. doi: 10.1109/TGRS.2002.802453.
[128] Braun A. DEM generation with Sentinel-1; 2020. http://step.esa.int/docs/tutorials/S1TBX%20DEM%20generation%20with%20Sentinel-1%20IW%20Tutorial.pd. Accessed 15 May 2020.
[129] Huang X. GITASAR; 2020. https://www.researchgate.net/project/A-Tiny-Synthetic-Aperture-Radar-Image-Processing-Tool. Accessed 15 Jun 2020.
[130] Pottier E, Ferro-Famil L, Fitrzyk M, Desnos Y-L. PolSARpro-BIO: the new scientific toolbox for ESA & third party fully polarimetric SAR missions. 12th European Conference on Synthetic Aperture Radar; 4–7 June 2018, Aachen: VDE Verlag; 2018.
[131] Grizonnet M, Michel J, Poughon V, Inglada J, Savinaud M, Cresson R. Orfeo ToolBox: open source processing of remote sensing images. Open geospatial data, softw stand. 2017;21:506. doi: 10.1186/s40965-017-0031-6.
[132] Rosen PA, Gurrola EM, Agram PS, Sacco GF, Lavalle M. The InSAR Scientific Computing Environment (ISCE): a Python framework for earth science. AGU Fall Meeting; 14–18 December 2015, San Francisco: American Geophysical Union (AGU); 2015. p. 1789.
[133] Morishita Y, Lazecky M, Wright TJ, Weiss JR, Elliott JR, Hooper A. LiCSBAS: an open-source InSAR time series analysis package integrated with the LiCSAR automated Sentinel-1 InSAR processor. Remote Sens. 2020;12:424. doi: 10.3390/RS12030424.
[134] Hooper A, Bekaert D, Spaans K, Arıkan M. Recent advances in SAR interferometry time series analysis for measuring crustal deformation. Tectonophysics. 2012;514:1–13.
[135] Truckenbrodt J, Cremer F, Baris I, Eberle J. PyroSAR: a framework for large-scale sar satellite data proessing. Proceedings of the 2019 Conference on Big Data from Space;

19–21 February 2019, Munich: European Space Agency (ESA); 2019. p. 197–200. doi: 10.2760/848593.
[136] Killough B. Overview of the open data cube initiative. IEEE International Geoscience and Remote Sensing Symposium; 22–27 July 2018, Valencia, Spain: Institute of Electrical and Electronics Engineers (IEEE); 2018. p. 8629–32.
[137] ASF. How to create a DEM using Sentinel-1 data; 2018. https://asf.alaska.edu/how-to/data-recipes/create-a-dem-using-sentinel-1-data/. Accessed 15 May 2020.
[138] Auer S, Burkert F, Gernhardt S. DEM generation with Matlab; 2016. https://eo-college.org/resource/dem_matlab/. Accessed 15 May 2020.
[139] Geymen A. Digital elevation model (DEM) generation using the SAR interferometry technique. Arab J Geosci. 2014;7:827–37. doi: 10.1007/s12517-012-0811-3.
[140] Atalay C, Sefercik UG. Comparison of Sentinel-1 and ALOS AW3D30 DSM potentials in a mountainous topography. Young Professionals Conference on Remote Sensing; 7–8 June 2018, Aachen, Germany: Institute of Electrical and Electronics Engineers (IEEE); 7–8 June 2018. p. 1–4.
[141] Sefercik UG, Buyuksalih G, Atalay C, Jacobsen K. Validation of Sentinel-1A and AW3D30 DSMs for the metropolitan area of Istanbul, Turkey. PFG. 2018;86:141–55. doi: 10.1007/s41064-018-0054-3.
[142] Ghannadi A, Enayati H, Khesali E. Generating digital elevation model of the earth using Sentinel-1 images and interferometry: Original title: تول ید مدل رقومی ارتفاعی زمین با استفاده از تصاویرسنتینل1- و تکنیک تداخل سنجی راداری. Sci Res Q Geograph Data. 2019;27:109–21. doi: 10.22131/sepehr.2019.34623.
[143] Ghannadi A, Enayati H, Khesali E. Interferometric Sentinel-1 DEM generation: a case study in Tehran, Iran; 7–10 October 2017. p. 1–4.
[144] Ghannadi MA, Alebooye S, Izadi M, Moradi A. A method for Sentinel-1 DEM outlier removal using 2-D Kalman filter. Geocarto Int. 2020;1–15. doi: 10.1080/10106049.2020.1815866.
[145] Mohammadi A, Bin Hamad B, Shahabi H. Extracting digital elevation model (DEM) from Sentinel-1 satellite imagery: case study a part of Cameron Highlands, Pahang, Malaysia. Int J Manag Appl Sci. 2018;4:109–14.
[146] Nikolakopoulos K, Kyriou A, Charalampopoulou V. DSM generation from Sentinel and COSMO-SkyMed data using interferometry and radargrammetry: a case study from Mykonos, Greece. In: Hadjimitsis DG, Themistocleous K, Michaelides S, Papadavid G, editors. 16 March 2015. Paphos, Cyprus: SPIE; 2015. p. 95350H. doi: 10.1117/12.2193977.
[147] Soni C, Chaudhary A, Sharma U, Sharma C. Satellite radar interferometry for DEM generation using Sentinel-1A imagery. In: Sharma MK, Dhaka VS, Perumal T, Dey N, Tavares JMRS, editors. Innovations in computational intelligence and computer vision. Singapore: Springer; 2021. p. 26–33. doi: 10.1007/978-981-15-6067-5_4.
[148] Sunu HA, Yuwono BD, Suprayogi A. DSM accuracy analysis of Semarang city using InSAR method using Sentinel-1 imagery: original title: analisis ketelitian DSM kota Semarang dengan metode InSAR Menggunakan citra Sentinel-1. J Geodesi Undip. 2019;8:17–26.
[149] Kakavas M, Nikolakopoulos KG, Kyriou A, Zagana H. Assessment of freely available DSMs for automatic karst feature detection. Arab J Geosci. 2018;11:388. doi: 10.1007/s12517-018-3654-8.
[150] Nonaka T, Asaka T, Iwashita K, Ogushi F. The relationships between errors of DEM and the height of ambiguity of Sentinel-1. IEEE International Geoscience and Remote Sensing Symposium; 28 July–02 September 2019. Yokohama: IEEE; 28 July–02 September 2019. p. 1725–8. doi: 10.1109/IGARSS.2019.8899305.
[151] Ullo SL, Angelino CV, Cicala L, Fiscante N, Addabbo P, Del Rosso MP, et al. SAR interferometry with open Sentinel-1 data for environmental measurements: the case of Ischia earthquake. IEEE International Conference on Environmental Engineering; 12–14 March 2018. Milano, Italy: IEEE; 2018. p. 1–8. doi: 10.1109/EE1.2018.8385270.
[152] Nikolakopoulos K, Kyriou A. Preliminary results of using Sentinel-1 SAR data for DSM generation. Eur J Geogr. 2015;6:52–68.
[153] Kumar P, Krishna AP. InSAR-based tree height estimation of hilly forest using multitemporal Radarsat-1 and Sentinel-1 SAR data. IEEE J Sel Top Appl Earth Observ Remote Sens. 2019;12:5147–52. doi: 10.1109/JSTARS.2019.2963443.
[154] Ortone Lois AS. Generation of DEMs in Los Glaciares National Park, in order to complement information related to elevation studies within the National Park and mass balance studies of Viedma Glacier and Frías Glacier: Original title: Generación de DEMs en el Parque Nacional Los Glaciares, con el objeto de complementar información relativa a estudios de elevación dentro del Parque Nacional y estudios de balance de masas del Glaciar Viedma y Glaciar Frías, 27–29 May 2020. Argentina: Buenos Aires; 2020. p. 1–15.
[155] Letsios V, Farasalis I, Stathakis D. InSAR DSM using Sentinel-1 and spatial data creation, 17–20 June 2019, Limassol, Cyprus: Association of Geographic Information Laboratories in Europe (AGILE); 2019. p. 1–4.
[156] Dabiri Z, Hölbling D, Abad L, Helgason JK, Sæmundsson Þ, Tiede D. Assessment of landslide-induced geomorphological changes in Hítardalur Valley, Iceland, using Sentinel-1 and Sentinel-2 data. Appl Sci. 2020;10:5848. doi: 10.3390/app10175848.
[157] Kyriou A, Nikolakopoulos K. Assessing the suitability of Sentinel-1 data for landslide mapping. Eur J Remote Sens. 2018;51:402–11. doi: 10.1080/22797254.2018.1444944.
[158] Nikolakopoulos KG, Kyriou A, Sabatakakis N, Anastassopoulos V. DSM generation using multiple radar data for relief change detection in North Peloponnese. In: Themistocleous K, Hadjimitsis DG, Michaelides S, Papadavid G, editors. 4 April 2016. Paphos, Cyprus: SPIE; 2016. p. 96880C. doi: 10.1117/12.2241124.
[159] Ahmadabadi A, Karam A, Saffari A, Yazdanpanah M. Estimation of surface and elevation displacement of Ardestan sand dunes using radar interferometry and spectral indices: Original title: برآورد جابجا یی مسطحاتی و ارتفاعی تپه های ماسه ای ریگ اردستان با استفاده از تداخل سنجی راداری و شاخص های طیفی. Quant Geomorphol Res. 2020;5(8):1–17.
[160] Yang H, Chen C, Chen S, Xi F, Liu Z. Radar interferometry using two imageswith different resolutions. IEEE Radar Conference (RadarConf), 22–26 April 2019. Boston; USA: Institute of Electrical and Electronics Engineers (IEEE); 2018. p. 1–5. doi: 10.1109/radar.2019.8835515.

[161] Choussiafis C, Karathanassi V, Nikolakopoulos K. Mosaic methods for improving the accuracy of interferometric based digital elevation models, 21–24 May 2012, Mykonos, Greece: European Association of Remote Sensing Laboratories (EARSeL); 2012. p. 1–9.
[162] Wang P. Applying two dimensional Kalman filtering for digital terrain modelling. Proc Int Arch Photogram, Remote Sensing, Spat Inf Sci. 1998;32(4):649–56.
[163] Morin P, Porter C, Cloutier M, Howat I, Noh M-J, Willis M, et al. ArcticDEM; a publically available, high resolution elevation model of the Arctic. EGUGA. 2016;18. EPSC2016-8396.
[164] Moran PAP. The interpretation of statistical maps. J R Stat Soc Ser B (Methodol). 1948;10:243–51.
[165] Helgason JK, Sæmundssson Þ, Drouin V, Jóhannesson T, Grímsdóttir H, Jónsson MH, et al. The Hítardalur landslide in West 2019. 21st EGU General Assembly; 2019. p. 1.
[166] Fitrzyk, M, Engdahl, M, Fernandez, D. ESA Copernicus Sentinel-1 Exploitation Activities. IEEE International Geoscience and Remote Sensing Symposium; 28 July–02 September 2019. Yokohama: IEEE; 28 July–02 September 2019. p. 5389–92. doi: 10.1109/IGARSS.2019.8898633.
[167] Chen R, Yu W, Wang R, Liu G, Shao Y. Integrated denoising and unwrapping of InSAR phase based on markov random fields. IEEE Trans Geosci Remote Sens. 2013;51:4473–85. doi: 10.1109/TGRS.2013.2268969.
[168] Ferretti A, Prati C, Rocca F. Multibaseline phase unwrapping for InSAR topography estimation. Il nuovo cimento C. 2001;24:159–76.
[169] Sica F, Pulella A, Nannini M, Pinheiro M, Rizzoli P. Repeat-pass SAR interferometry for land cover classification: a methodology using Sentinel-1 Short-Time-Series. Remote Sens Environ. 2019;232:111277. doi: 10.1016/j.rse.2019.111277.
[170] Wegmüller U, Santoro M, Werner CL, Cartus O. On the estimation and interpretation of Sentinel-1 TOPS InSAR coherence. FRINGE workshop; 23–27 March 2015, Frascati: European Space Agency (ESA); 2015. p. 1–4.
[171] Zebker HA. Snaphu: statistical-cost, network-flow algorithm for phase unwrapping, version 2.0.4 (August 2020); 2020. https://web.stanford.edu/group/radar/softwareandlinks/sw/snaphu/README_releasenotes.txt. Accessed 3 Dec 2020.
[172] ASF. ASF baseline tool; 2020. https://baseline.asf.alaska.edu. Accessed 15 May 2020.
[173] Hanssen R. Assessment of the role of atmospheric heterogeneities in ERS tandem SAR interferometry. Delft Univ, Delft, Netherlands, DEOS Rep. 1998;12:137.
[174] Yu C, Li Z, Penna NT, Crippa P. Generic atmospheric correction model for interferometric synthetic aperture radar observations. J Geophys Res Solid Earth. 2018;123:9202–22. doi: 10.1029/2017JB015305.
[175] Eineder M. Problems and solutions for InSAR digital elevation model generation of mountainous terrain. FRINGE workshop; 1–5 December 2003, Frascati: European Space Agency (ESA); 2003. p. 1–9.
[176] Deo R, Rossi C, Eineder M, Fritz T, Rao YS. Framework for fusion of ascending and descending pass TanDEM-X raw DEMs. IEEE J Sel Top Appl Earth Observ Remote Sens. 2015;8:3347–55.
[177] ESA. Level-1 product formatting; 2020. https://sentinel.esa.int/web/sentinel/technical-guides/sentinel-1-sar/products-algorithms/level-1-product-formatting. Accessed 15 Nov 2020.
[178] Höhle J, Höhle M. Accuracy assessment of digital elevation models by means of robust statistical methods. ISPRS J Photogram Remote Sens. 2009;64:398–406.
[179] Uuemaa E, Ahi S, Montibeller B, Muru M, Kmoch A. Vertical accuracy of freely available global digital elevation models (ASTER, AW3D30, MERIT, TanDEM-X, SRTM, and NASADEM). Remote Sens. 2020;12:3482. doi: 10.3390/rs12213482.
[180] Yoëli P. The mechanisation of analytical hill shading. Cartographic J. 1967;4:82–8. doi: 10.1179/caj.1967.4.2.82.
[181] Podobnikar T. Methods for visual quality assessment of a digital terrain model. Sapiens. 2019;2:1–10.
[182] Teillet PM, Horler D, O'Neill NT. Calibration, validation, and quality assurance in remote sensing: a new paradigm. Can J Remote Sens. 1997;23:401–14. doi: 10.1080/07038992.1997.10855225.
[183] Mestre-Quereda A, Lopez-Sanchez JM, Vicente-Guijalba F, Jacob AW, Engdahl ME. Time-series of Sentinel-1 interferometric coherence and backscatter for crop-type mapping. IEEE J Sel Top Appl Earth Observ Remote Sens. 2020;13:4070–84.
[184] Devaraj S, Yarrakula K. Assessment of topographical and atmospheric errors in Sentinel 1 derived DInSAR. Geocarto Int. 2020;1–17. doi: 10.1080/10106049.2020.1822926.
[185] Bekaert D, Walters RJ, Wright TJ, Hooper AJ, Parker DJ. Statistical comparison of InSAR tropospheric correction techniques. Remote Sens Environ. 2015;170:40–7. doi: 10.1016/j.rse.2015.08.035.
[186] van Niel TG, McVicar TR, Li L, Gallant JC, Yang Q. The impact of misregistration on SRTM and DEM image differences. Remote Sens Environ. 2008;112:2430–42. doi: 10.1016/j.rse.2007.11.003.
[187] Willmott CJ, Matsuura K. Advantages of the mean absolute error (MAE) over the root mean square error (RMSE) in assessing average model performance. Clim Res. 2005;30:79–82. doi: 10.3354/cr030079.
[188] Story M, Congalton RG. Accuracy assessment: a user's perspective. Photogram Eng Remote Sens. 1986;52:397–9.
[189] Congalton RG. Accuracy assessment and validation of remotely sensed and other spatial information. Int J Wildland Fire. 2001;10:321–8.
[190] Liu H, Jezek KC. Investigating DEM error patterns by directional variograms and Fourier analysis. Geograph Anal. 1999;31:249–66.
[191] Wechsler SP. Perceptions of digital elevation model uncertainty by DEM users. Urisa-Washington DC. 2003;15:57–64.
[192] Wechsler SP, Kroll CN. Quantifying DEM uncertainty and its effect on topographic parameters. Photogram Eng Remote Sens. 2006;72:1081–90.
[193] Crosetto M, Budillon A, Johnsy A, Schirinzi G, Devanthéry N, Monserrat O, et al. Urban monitoring based on Sentinel-1 data using permanent scatterer interferometry and SAR tomography. Int Arch Photogramm Remote Sens Spat Inf Sci. 2018;XLII(3):235–8. doi: 10.5194/isprs-archives-XLII-3-235-2018.
[194] Nannini M, Prats-Iraola P, Scheiber R, Yague-Martinez N, Minati M, Vecchioli V, et al. Sentinel-1 mission: Results of the InSARap project. 11th European Conference on Synthetic Aperture

Radar; 6–9 June 2016. Hamburg, Germany: VDE Verlag; 2016. p. 1–4.
[195] Giudici D, Mapelli D, Rocca F. Exploring the potential of Sentinel-1 constellation in tandem and bi-static configurations. 12th European Conference on Synthetic Aperture Radar; 4–7 June 2018. Aachen: VDE Verlag; 2018. p. 1–6.
[196] Minh DHT, Hanssen R, Rocca F. Radar interferometry: 20 years of development in time series techniques and future perspectives. Remote Sens. 2020;12:1364. doi: 10.3390/rs12091364.
[197] Braun A. Radar satellite imagery for humanitarian response. Bridging the gap between technology and application. Doctoral dissertation/PhD. Tübingen, Germany: University of Tübingen; 2018.
[198] ASF. Sentinel-1 Level 1 SLC data coverage; 2020. https://asf.alaska.edu/data-sets/sar-data-sets/sentinel-1/sentinel-1-acquisition-maps/. Accessed 15 Jun 2020.

Appendix

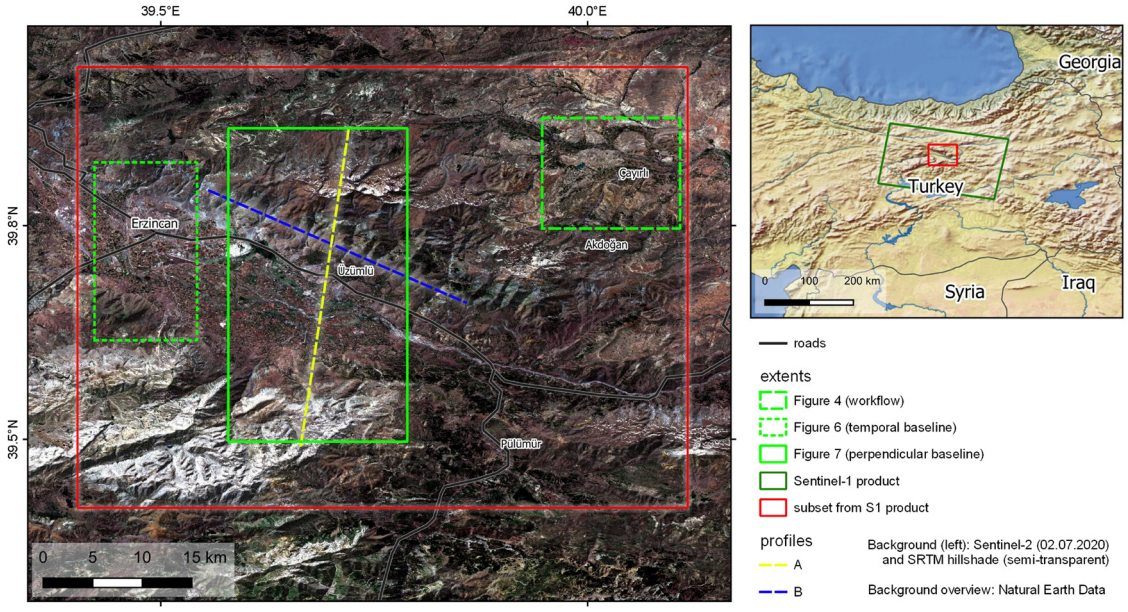

Figure A1: Overview on the study area (Section 2.1).